



UiT The Arctic University of Norway

Faculty of Science and Technology
Department of Physics and Technology

Wind resource assessment using LiDAR

Oluwatimilehin Israel Osunlola

FYS-3900: Master's thesis in physics – 60 ECTS

June 2024

Abstract

This thesis presents a comprehensive wind resource assessment for the expansion of the Fakken wind park in Norway, leveraging Light Detection and Ranging (LiDAR) technology. The study, conducted from December 2022 to June 2023, aims to detail LiDAR measurement methodologies, analyze collected data, and estimate wind energy production.

Key findings reveal predominant wind directions and speeds, with January 2023 exhibiting peak speeds. While challenges include deviations between LiDAR and met mast data, promising correlations suggest LiDAR's potential as a wind resource assessment tool. Statistical evaluations and Weibull distribution analyses support the reliability of LiDAR data for wind energy estimation.

Future research directions include validating LiDAR performance over longer periods and refining data processing techniques for enhanced accuracy.

This thesis emphasizes the importance of comprehensive wind resource assessment for informed wind energy development decisions, with LiDAR technology offering promising opportunities for accuracy and efficiency.

Acknowledgements

This thesis journey has been a testament to perseverance, diligence, and dedication. While the path wasn't always smooth, every stumble and fall served as a moment of profound learning and self-reflection.

First and foremost, I express my deepest gratitude to God for His unwavering guidance and support throughout this endeavor. I am immensely grateful to my supervisor, Yngve, whose patience and expertise have been invaluable. His willingness to delve into every concept with meticulous detail has been instrumental in shaping this work.

To my family, thank you for being my pillars of strength, offering unwavering support, prayers, and motivating words during both the highs and lows of this journey.

A heartfelt appreciation goes to Tausi for her unwavering companionship and steadfast support. Her presence, encouragement, and willingness to lend an ear during challenging times have been a source of immense comfort.

I extend my gratitude to the entire staff of the Department of Physics and Technology at UiT, as well as my fellow students, for creating an enriching and collaborative environment. Your camaraderie, encouragement, and shared experiences have made this journey both enjoyable and rewarding.

Table of Contents

Abstract	iv
Acknowledgements	v
List of Tables.....	x
List of Figures	xi
Abbreviations	xiv
1 Introduction	1
1.1 Background	1
1.2 Former research.....	2
1.3 Aim of Thesis	4
1.4 Outline of Thesis	5
2 Theoretical Background	6
2.1 Wind in the atmosphere.....	6
2.1.1 Coriolis effect on wind	6
2.1.2 Effect of pressure systems.....	8
2.1.3 Vertical distribution of wind	10
2.1.4 Atmospheric stability	15
2.1.5 Atmospheric motions	17
2.2 Complex terrain.....	18
2.3 Wind phenomena in complex terrain	20
2.4 Wind Energy	21
2.4.1 Wind power	21
2.4.2 Wind turbine and efficiency.....	25
2.4.3 Wake losses	26
2.4.4 Micro-siting.....	28
2.5 Wind data visualization.....	29

2.5.1	Wind roses	29
2.5.2	Histogram of wind speeds	30
2.5.3	Weibull distribution function	31
2.6	Evaluating models	32
2.7	Light Detection and Ranging (LiDAR).....	34
3	Data and Methods.....	39
3.1	Description of Fakken wind park	39
3.2	LiDAR Setup.....	42
3.2.1	Scanning LiDAR scan patterns	43
3.3	Data	47
3.3.1	LiDAR data processing and cleaning.....	47
4	Results and Discussion.....	49
4.1	Wind rose from fixed LiDAR scans.....	49
4.2	Wind rose for In-situ measurements from meteorological mast	50
4.3	Wind rose for In-situ measurements from nearest turbine to LiDAR 34.....	51
4.4	Wind rose for In-situ measurements from nearest turbine to LiDAR 40.....	52
4.5	Correlation Test.....	53
4.5.1	Wind speed time series correlation for LiDAR wind data and met-mast (January 2023).....	53
4.5.2	Wind speed time series correlation for LiDAR wind data and met-mast (February 2023).....	55
4.6	Histogram of wind speed and Weibull distribution plot for LiDAR wind speed data and met-mast speed data	57
4.7	Estimation of wind energy production from LiDAR wind data.....	59
4.7.1	Using WASP for turbine siting at Fakken II.....	64
5	Conclusion.....	67
5.1	Summary and key findings.....	67

5.2 Future work	69
Bibliography.....	70
Appendix A	77
Appendix B	80

List of Tables

Table 2-1 – Approximate surface roughness length for different terrain types (Saheb et al., 2014). 13

Table 2-2 – Power law exponent values for different types of terrain (Bechrakis & Sparis, 2000). 14

Table 2-3 – European locations where experiments were conducted and their corresponding complex terrain feature. 19

Table 2-4: Measured parameters of a Doppler wind LiDAR (Reitebuch & Hardesty, 2021). 37

Table 3-1: Locations of LiDARs, fixed point in Fakken II, closest turbines to LiDARs and fixed point in various coordinate systems. 43

Table 4-1: Statistical evaluation of the estimated energy production from the model and observed data. 61

Table 4-2: Results of statistical evaluation after applying data handling techniques..... 62

List of Figures

Figure 2-1: Resultant geostrophic wind from pressure gradient force (PGF) and Coriolis force (F_c) (Manwell et al., 2010b). 7

Figure 2-2: Atmospheric circulations with the convection cells (Wei, 2010). 7

Figure 2-3: Concept of low- and high-pressure systems. 9

Figure 2-4: Low- and high-pressure systems in Earth’s northern hemisphere (Spiridonov et al., 2021b). 10

Figure 2-5: Changes of wind speed with height (Van Der Tempel, 2006). 10

Figure 2-6: Atmospheric boundary layer (ABL) schemes. 11

Figure 2-7: Wind profiles in neutral, unstable and stable conditions (Petersen et al., 1997). 16

Figure 2-8: Cases of complex terrain features (Abdi & Bitsuamlak, 2014). 18

Figure 2-9: Complex terrains showing topography and elevation features. 19

Figure 2-10: Formation of gap winds. 21

Figure 2-11: Stream tube depicting mass airflow through an area of interest (Gasch & Twele, 2011a). 22

Figure 2-12: Power curve of a Vestas V90-3.0 turbine (Vestas, 2007). 25

Figure 2-13: Three distinct descriptions of wind turbine wakes. Left: Condensation plumes produced by turbulence within turbine wakes in the Horns Rev 2 offshore wind park (Hasager et al., 2017). Middle: Wind speed deficits within turbine wakes from a complex wind field measured with a Doppler Ka-band radar (Texas, 2014). Right: Simulation of wind speed deficits for the Lillgrund offshore wind project using the Jensen model with a wake decay constant of 0.04 (Smith et al., 2012). 27

Figure 2-14: Example of a wind rose diagram (Chavan et al., 2017). 29

Figure 2-15: Sample of a typical histogram showing wind speed frequencies. 30

Figure 2-16: Example of a Weibull distribution function for mean wind speed U of 6 m/s (Manwell et al., 2010b). 32

Figure 2-17: Schematic of the Doppler wind LiDAR measurement principle. Left: LiDAR beam interacting with aerosol particles. Right: Idealised distribution of aerosol Doppler velocities over the LiDAR volume based on the frequency shift between emitted and returned laser signal (Christiane, 2024). 36

Figure 2-18: Polar coordinates (Left): azimuth angle, α , elevation angle, δ , or zenith angle, θ_z and range, r . Right: Projection of radial velocity in a vertical plane along the horizontal x-axis (u and w). The combinations of u and w along the gray striped line perpendicular to the LiDAR’s beam orientation resulting in radial velocity (Christiane, 2024). 36

Figure 2-19: External view and features of the Leosphere WindCube100s (WLS100s) scanning LiDAR (Leosphere, 2023). 38

Figure 3-1: Map of the region with the Fakken wind park in red square.	39
Figure 3-2: Terrain height of the topography around Fakken wind park (Norgeskart, 2023).	40
Figure 3-3: Siting of wind turbines in Fakken I	41
Figure 3-4: Planning for Fakken II. Left: New site location for Fakken II. Right: Proposed siting of new turbines in Fakken II	41
Figure 3-5: Placement of LiDAR34, LiDAR40 and Fixed point in Fakken II	42
Figure 3-6: Schematic overview of the line-of-sight projection of the wind speed (van Dooren, 2022).	44
Figure 3-7: PPI scan with varying azimuth angles and a fixed elevation angle (Julia, 2022).	45
Figure 3-8: Layout of a Doppler beam swing (DBS) LiDAR scan (van Dooren, 2022)	46
Figure 3-9: Filtering of granular noise from radial velocity vr observations.	48
Figure 4-1: Left: Wind rose showing wind resource at the Fakken II fixed point for January 2023. Right: Wind rose showing wind resource at the Fakken II at fixed point for February 2023.	49
Figure 4-2: Wind rose showing wind resource at Fakken II fixed point for March 2023.	49
Figure 4-3: Left: Wind rose showing wind resource at Fakken I met-mast for January 2023. Right: Wind rose showing wind resource at Fakken II met-mast for February 2023.	50
Figure 4-4: Wind rose showing wind resource at Fakken I met-mast for March 2023.	50
Figure 4-5: Left: Wind rose showing wind resource at WTG10 turbine for January 2023. Right: Wind rose showing wind resource at WTG10 turbine for February 2023.	51
Figure 4-6: Wind rose showing wind resource at WTG10 turbine for March 2023.	51
Figure 4-7: Left: Wind rose showing wind resource at WTG15 turbine for January 2023. Right: Wind rose showing wind resource at WTG15 turbine for February 2023.	52
Figure 4-8: Wind rose showing wind resource at WTG15 turbine for March 2023.	52
Figure 4-9: Time series correlation between wind speed from LiDAR and wind speed from met-mast.	53
Figure 4-10: Correlation matrix between LiDAR data sample and Met-Mast data sample.	54
Figure 4-11: Time series correlation plot for a week in January 2023	55
Figure 4-12: Time series correlation between wind speed from LiDAR and wind speed from met-mast.	55
Figure 4-13: Time series correlation plot for a week in February 2023.	56
Figure 4-14: Left: Weibull distribution for LiDAR wind speed data. Right: Histogram plot of LiDAR wind speed data	57
Figure 4-15: Left: Weibull distribution for met-mast wind speed data. Right: Histogram plot of met-mast wind speed data	58

Figure 4-16: Energy production within January to March 2023 for each turbine at Fakken I.	59
Figure 4-16: Estimated energy production within January to March 2023 for Turbine F at Fakken II.	60
Figure 4-17: Resource grid from WAsP over Fakken I and Fakken II (Bjugg, 2023).	64
Figure 4-18: Resource grid from WAsP showing wind roses indicating gross AEP and potential wake losses (Bjugg, 2023).	65
Figure 4-19: Effect of repositioning turbines at Fakken II adding to the yearly energy production from a sampled 2017 data (Bjugg, 2023).	66

Abbreviations

ABL – Atmospheric Boundary Layer

AGL – Above Ground Level

AEP – Annual Energy Production

CFD – Computational Fluid Dynamics

CI– Confidence Index

CNR – Carrier to Noise Ratio

CW – Continuous Wave

GIS – Geographic Information Systems

GW – Gigawatt

GWh – Gigawatt hour

KW – Kilowatt

LiDAR – Light Detection and Ranging

LOS – Line of Sight

MAE – Mean Absolute Error

MAPE – Mean Absolute Percentage Error

MW – Megawatt

MWh – Megawatt hour

NaN – Not a Number

RANS – Reynolds Averaged Navier Stokes

RIX – Ruggedness Index

RMSE – Root Mean Square Error

ROI – Return on Investment

SNR – Signal to Noise Ratio

SODAR – Sonic Detection and Ranging

WAsP – Wind Atlas Analysis and Application Program

1 Introduction

1.1 Background

The world energy demand is on the rise being driven by factors such as population increase, industrialization, and technological advancements. This increasing demand comes with significant environmental concerns, particularly in relation to the reliance on conventional energy sources like fossil fuels. This reliance imposes a burden on our environment, primarily through the emission of carbon dioxide (CO₂) aggravating climate change and environmental degradation (Panwar et al., 2011).

The transition to utilizing renewable energy sources and adopting ethical energy production practices offers a viable solution to address these pressing issues. Among renewable energy sources, wind power has emerged as a primary contender, with its energy capacity projected to steadily grow despite challenges with high material costs and supply chain constraint. According to (IEA, 2024), the renewable electricity capacity for wind power is estimated to rise from 498GW to 700GW within 2023 to 2028. This growth shows the pivotal role of wind energy in the global shift towards renewable energy, thereby aligning with efforts to reduce reliance on fossil fuels.

To efficiently harness wind energy, precise and comprehensive wind measurements also known as wind resource assessment, are essential. Traditionally, these measurements have been conducted using a cup anemometer in conjunction with a wind vane, typically producing a 2D wind speed vector in the horizontal plane (van Dooren, 2022). This setup is commonly found on meteorological towers/meteorological masts also known as met masts in the wind energy sector (Neto & Castelao, 2023; Vasiljević et al., 2020). Nowadays, there is an increasing acceptance of using Light Detection and Ranging (LiDAR) technology as an alternative to the traditional mast-based sensors such as cup anemometers and ultrasonic anemometers (van Dooren, 2022). LiDAR offers several advantages over the traditional method. This remote sensing device can measure wind speeds at heights from few meters to multiple kilometers. Additionally, LiDAR is easily deployable, cost-effective, and does not require a setup permit (Menke et al., 2019).

Norway, with its extensive coastlines and complex terrain, boasts of significant wind power potential that remains largely untapped. The country's unique geography presents both

challenges and opportunities for harnessing wind energy effectively. The wind parks located around complex terrain close to the coastline usually offer promising conditions for wind energy development but pose a challenge for accurate wind resource assessment (Berge et al., 2006).

As LiDAR becomes increasingly utilized for wind measurements in complex terrain, certain challenges persist due to the non-homogenous nature of wind flow, posing difficulties in data reconstruction. Moreover, the heterogeneity resulting from wind flow in complex terrain diminishes the representativeness of measurements obtained from traditional anemometers (Bradley et al., 2015; Clifton et al., 2018). Addressing these challenges, common approaches for wind resource assessment in complex terrain include integrating LiDAR and met-mast measurements with appropriate flow models. Additionally, deploying two or more LiDARs with scanning capabilities enables comprehensive assessment of wind conditions over a large area (Clifton et al., 2018; Vasiljević et al., 2020).

1.2 Former research

This subsection will provide an overview of the existing body of research related to wind measurements and LiDAR technology. The aim is to highlight the importance of reviewing former research to identify gaps, build upon existing knowledge and situate this study within the broader research landscape.

The detailed knowledge of wind resources is essential in the developmental and operational stages of a wind park site. Numerous studies have investigated wind measurements using established instruments such as cup anemometers, sonic anemometers, and wind vanes. These instruments are commonly mounted on the nacelle wind turbines or on nearby masts at the hub height of the wind turbines (Allik et al., 2014; Lang & McKeogh, 2011). The rationale for positioning the cup anemometers at a height close to the wind turbine is to ensure an undistorted wind flow is measured over the site and this is vital for the turbine micro-siting (Kim et al., 2016; Lang & McKeogh, 2011).

A study by (Allik et al., 2014) was conducted to investigate the influence of the wind turbine rotors on the wind data measurements obtained from the nacelle-mounted anemometers. The

study took place at wind park sites located in North Estonia and the Estonian island, where two 10kW turbines were examined. These turbines had hub heights of 18 meters and 16 meters, with two different anemometers placed on each turbine's nacelle. To compare and validate the data, reference measurement was obtained from two measurement masts positioned at 2-4 times of the wind turbine diameter. These masts were equipped with three anemometers at multiple heights (18 m, 26 m, 40 m) and a wind direction sensor at a height of 40 meters. The study concluded that the rotation of the rotor blades significantly impacts the wind data measurements from the nacelle-mounted anemometers during the wind turbine operation. As a result, the average wind speeds recorded from the nacelle-mounted anemometers were significantly lower than those from reference mast anemometers. Despite this difference, strong correlations were observed between nacelle-mounted anemometers readings and the reference data (Allik et al., 2014).

In another article published by (Schneemann et al., 2014), the performance of a 2D multi-LiDAR was assessed through comparison with a met mast cup anemometer, focusing on average wind speed, wind direction, and turbulence intensity measurements. The measurement campaign took place in the north of Germany using two long-range Doppler LiDARs and anemometers, along with wind vanes, which were mounted on a 100 m high meteorological mast. The results showed a good correlation between both wind speeds and directions, as well as turbulence measurements in free sectors. However, some shortcomings remain in applying LiDAR in turbulence measurement, although there is significant potential for turbulence analysis (Sathe & Mann, 2013; van Dooren, 2022).

In an article by (Kim et al., 2016), a measurement campaign was conducted to evaluate the reliability of ground-based LiDAR for wind measurements compared to met-masts across various terrain conditions, focusing on the impact of terrain complexity on measurement accuracy. Three measurement sites in Korea were evaluated using a Ruggedness Index (RIX), with computational fluid dynamics (CFD) analysis conducted at one of the sites with the highest RIX which is characterized as a complex terrain. Data filtering was implemented between LiDAR and met-mast measurements to ensure data comparability. The study concluded that while there is strong correlation between wind measurements from LiDAR and metrological masts, LiDARs have a high chance of wind speed errors over complex terrain. However,

techniques such as CFD analysis and LiDAR-based estimation of detailed wind profiles offer potential solutions to correct these measurement biases (Clifton et al., 2018; Kim et al., 2016).

In conclusion, exploring existing research in wind measurement methodologies and LiDAR technology reveals a dynamic landscape marked by both traditional instruments used for wind measurement and cutting-edge innovations. From the studies examined on this subject it is seen that there is a complex interaction between wind dynamics, measurement techniques, and environmental factors.

These investigations emphasize the importance of comprehensive wind resource assessment for effective wind park development and operation. While traditional instruments remain integral in the wind energy sector, the emergence of LiDAR technology presents promising opportunities for enhanced accuracy and efficiency.

1.3 Aim of Thesis

The aim of this thesis is to conduct a comprehensive assessment of wind resources for the expansion of the Fakken wind park, situated in Norway. Established in 2012, the Fakken wind park features 18 Vesta V90 3MW wind turbines with an average yearly production of 138GWh, owned by Troms Kraft Production (Troms, 06.11.2023). Considering the potential for expansion, a collaborative effort between UiT, UiB, and Troms Kraft in spring 2023 involved the installation of two pulsed long-range Doppler LiDARs within the park's terrain to measure wind phenomena.

Wind resource assessment is crucial prior to wind power plant construction, often initiated by identifying potential sites and conducting measurement campaigns using meteorological masts. The measurement campaign done on the Fakken wind park spanned from December 2022 to June 2023. This thesis primary objectives are to detail the methodologies employed to: describe LiDAR measurement for wind, analyze data from the LiDAR at the Fakken wind park, analyze wind profiles and resources, and estimate wind energy production.

1.4 Outline of Thesis

Including the introduction section, this thesis is structured to consist of six chapters: Theoretical Background, Data and Methods, Results and Discussion then followed by the section of Conclusion and Future Work

Chapter 2: - This chapter offers a theoretical foundation for the research methodology, focusing on concepts such as wind generation, vertical wind distribution, wind energy principles, wind turbine operations, wake losses, micro-siting strategies, visualization methods for wind data, and the significance of LiDAR technology.

Chapter 3: - This chapter provides a comprehensive overview of the data collection process involving LiDAR, along with an exploration of statistical signal processing techniques applied to wind measurements. It delves into the filtering methodology utilized for processing LiDAR-measured data employed in the research. Additionally, it discusses the experimental setup deployed on-site and the various data analysis methods employed to extract insights from the collected data.

Chapter 4: - In this chapter, the focus is on presenting and discussing the results obtained from the study. It begins with an analysis of wind measurements derived from LiDAR scans, providing insights into the spatial and temporal variations of wind patterns. Following this, the correlation between LiDAR measurements and those obtained from the met mast is examined, shedding light on the consistency and reliability of LiDAR data. Finally, the chapter explores the estimation of wind energy production based on LiDAR wind measurements, offering valuable insights into the potential energy yield of the studied site.

Chapter 5: - This concluding chapter will include a comprehensive summary of the study's findings and key insights. Also, the chapter will offer some reflections on the implications of the findings and their significance in a greater context. Furthermore, this chapter will outline potential avenues for future research and development in this field.

2 Theoretical Background

2.1 Wind in the atmosphere

Renewable energy harnessed from the Earth's wind primarily originates from the sun, which drives global wind patterns. The uneven heating of the Earth's surface by solar radiation creates pressure differences, resulting in the generation of winds (Manwell et al., 2010b; Wei, 2010). As the Earth orbits the sun, the equatorial regions receive solar radiation more directly, causing greater heating compared to the polar regions. This discrepancy in heating establishes a horizontal temperature gradient from the equator to the poles, thereby creating a horizontal pressure gradient that leads to a pressure gradient force (Ahrens, 2019; Wei, 2010).

This pressure gradient force (PGF), which is vertically dominant, can be counteracted by the downward gravitational force. Additionally, other forces influencing the horizontal movement of air include the Coriolis force due to Earth's rotation and frictional forces acting on the Earth's surface (Ahrens, 2019; Manwell et al., 2010b). The pressure gradient force drives the movement of air, with the pressure force on air per unit mass denoted as F_p is defined as:

$$F_p = \frac{-1}{\rho} \frac{\partial \rho}{\partial n} \quad (2.1)$$

where ρ represents air density, and n represents the direction or distance normal to lines of constant pressure also known as isobars. The term $\frac{\partial \rho}{\partial n}$ denotes the pressure gradient normal to the lines of constant pressure, indicating the rate of change of air density with respect to distance normal to the isobars (Manwell et al., 2010b). When the air is solely influenced by the pressure gradient force, wind flows from regions of higher pressure to low pressure. However, this phenomenon changes due to the Coriolis force, which deflects the path of the air (Ahrens, 2019).

2.1.1 Coriolis effect on wind

The Coriolis force (F_c) is a fictitious force resulting from the Earth's rotation, which deflects the direction of atmospheric movements (Wei, 2010). In the Northern Hemisphere, winds are deflected to the right, while in the Southern Hemisphere, they are deflected to the left (Ahrens, 2019; Persson, 1998; Wei, 2010). The magnitude of the Coriolis force varies with the Earth's latitude, being zero at the equator and reaching its maximum at the poles. Additionally, the

Coriolis force is influenced by the Earth’s rotation and wind speed; slower winds experience minimal deflection, while stronger winds are deflected more (Ahrens, 2019; Wei, 2010).

This Coriolis force can be expressed as:

$$F_c = fU \tag{2.2}$$

where U is the wind speed and f is the Coriolis parameter given by $f = 2\omega \sin(\phi)$. Here, ϕ represents the Earth’s latitude and ω represents the angular rotation of the Earth. It is apparent from the expression that the magnitude of the Coriolis force depends on both wind speed and latitude. Additionally, the direction of the Coriolis force is perpendicular to the direction of air motion.

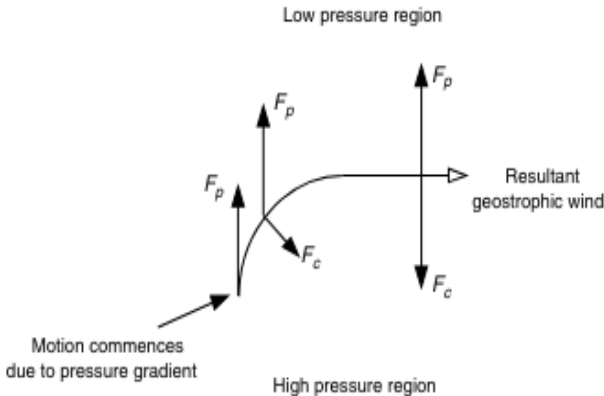


Figure 2-1: Resultant geostrophic wind from pressure gradient force (PGF) and Coriolis force (F_c) (Manwell et al., 2010b).

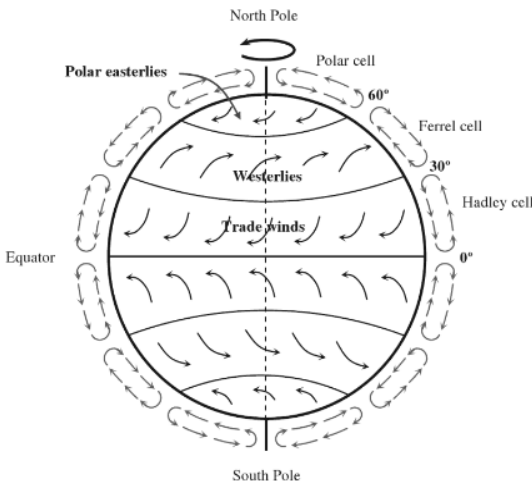


Figure 2-2: Atmospheric circulations with the convection cells (Wei, 2010).

In Figure 2-1, the combined influence of the pressure gradient force (PGF) and Coriolis force (F_c) results in the geostrophic wind, which flows parallel to isobars (Manwell et al., 2010b). In the Northern Hemisphere, the geostrophic wind deflects to the left under lower pressure and to the right under higher pressure. When airflow becomes geostrophic, isobars ideally become straight and evenly spaced, with wind speed remaining relatively constant. However, in reality, isobars are rarely perfectly straight or uniformly spaced, and the geostrophic wind serves as an approximation of actual wind behavior, aiding in understanding wind patterns aloft (Ahrens, 2019).

In large-scale atmospheric movements, the combined effects of the pressure gradient force (PGF) and the Coriolis force (F_c) lead to the division of the single meridional cell into three distinct convectional cells in each hemisphere. These convection cells, depicted in Figure 2-2, include the Hadley cell, the Ferrel cell, and the Polar cell. Each cell exhibits unique circulation patterns driven by differential heating and the Earth's rotation (Wei, 2010).

2.1.2 Effect of pressure systems

Pressure systems are regions that indicate variations in atmospheric pressure within an airflow. High- and low-pressure systems are the two forms of these pressure systems. They are formed by atmospheric processes such as temperature differences between the atmosphere, water and land, upper-level disturbances and differential solar heating (Spiridonov et al., 2021a). The distribution of these pressure systems defines the local weather within an area. According to (Holton, 2004; Martin, 2006; Thompson, 2002; Wallace & Hobbs, 2006a) low-pressure systems (also known as cyclone) and high-pressure systems (also known as anticyclone) are used to describe organized atmospheric systems characterized by circular flow areas with low and high atmospheric pressure, respectively. Cyclones are typically associated with unstable atmospheric conditions and can be identified on weather charts by tightly spaced isobars, while anticyclones occur where the weather is dominated by stable conditions, characterized by a large area of widely spaced isobars (Spiridonov et al., 2021b).

Winds in the low-pressure system (LPS) within the Earth's northern hemisphere blow in a counterclockwise direction, while they blow in a clockwise direction in the southern hemisphere. When air flows into a low-pressure area from all directions, the Coriolis force causes the cyclonic flow to deflect to the right, creating a counterclockwise rotation around the

center of the low-pressure system, as shown in Figure 2-4a. Convergence occurs at the bottom area of the LPS, where airflow from different directions collides near the center and is forced to rise (Spiridonov et al., 2021b). This rising air cools and condenses, leading to the formation of large clouds, strong winds and heavy rainfall, as illustrated in Figure 2-3. Near the Earth's surface, friction is dominant and causes a redistribution of airflow within the atmosphere by changing its direction. The movement of air occurs at an angle normal to the low-pressure area, affirming the phenomenon of the resultant wind blowing in the counterclockwise direction in the northern hemisphere (Spiridonov et al., 2021b).

In a high-pressure system (HPS), winds blow in a clockwise direction in the Earth's northern hemisphere, and blow in a counterclockwise direction in the southern hemisphere. The anticyclonic air typically sinks, creating an area of higher pressure at the surface. As illustrated in Figure 2-3, cloud formation is constrained under these conditions, and winds are often quite light, resulting in stable and sunny weather. There is convergence in the upper layers, which causes air to descend to the surface of high-pressure areas. As seen in Figure 2-4b, the air diverges at the center of the high-pressure system, and the Coriolis force deflects the air to the right, creating a clockwise rotation around the center of the system (Spiridonov et al., 2021b).

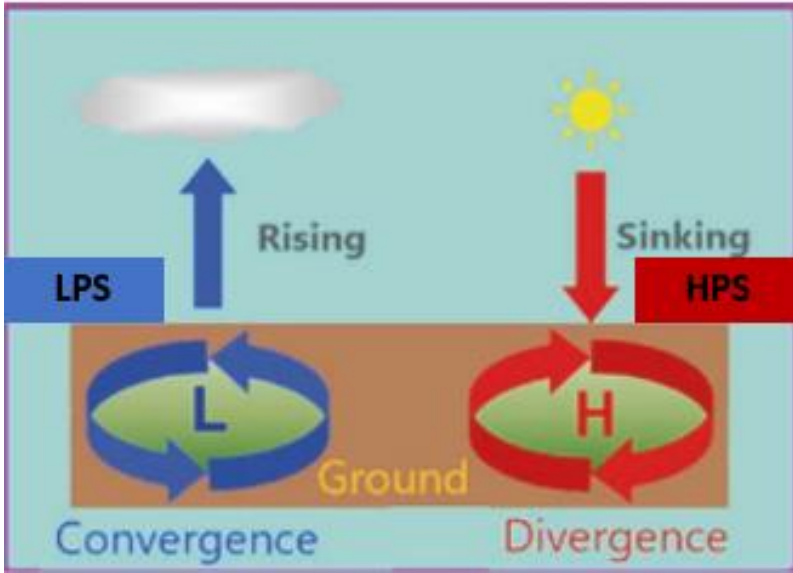
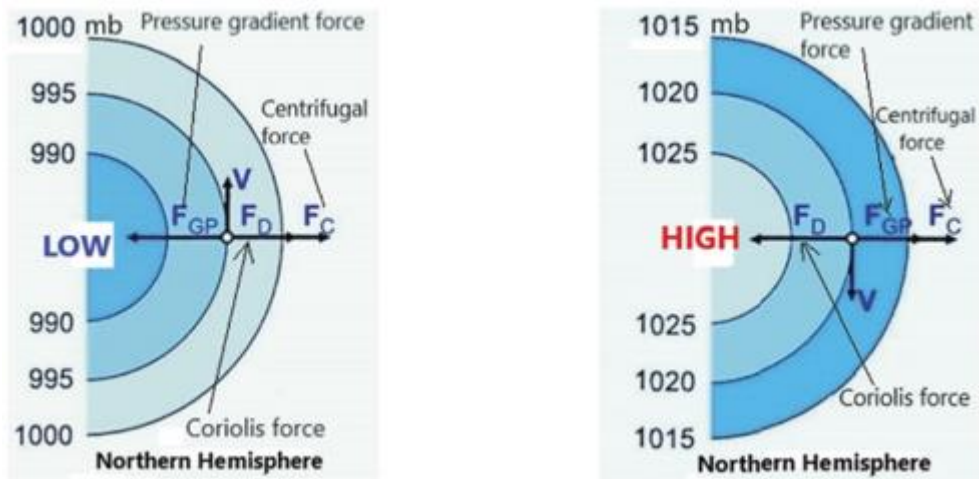


Figure 2-3: Concept of low- and high-pressure systems.



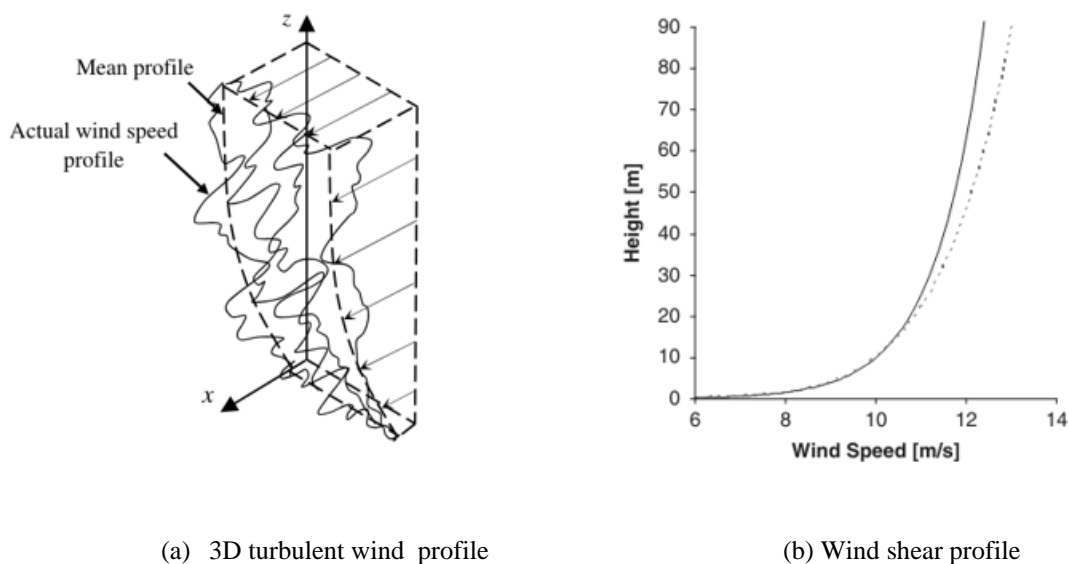
(a) Air flow in the cyclone (low-pressure system)

(b) Air flow in an anticyclone (high-pressure system)

Figure 2-4: Low- and high-pressure systems in Earth’s northern hemisphere (Spiridonov et al., 2021b).

2.1.3 Vertical distribution of wind

The vertical distribution of wind is an essential aspect of atmospheric dynamics. Wind velocity fluctuates across different locations and over time. As shown in Figure 2-5a, the actual wind speed and direction tends to deviate from their average values because of turbulence. From Figure 2-5b, it is noticeable that the wind speed increases with height which is a phenomenon known as wind shear or vertical wind profile (Van Der Tempel, 2006).



(a) 3D turbulent wind profile

(b) Wind shear profile

Figure 2-5: Changes of wind speed with height (Van Der Tempel, 2006).

The atmospheric boundary layer (ABL), estimated to be 0.3 to 3km thick and is placed in the lower part of the Earth’s atmosphere, extending up to 2km above the surface. The air flow in this layer is influenced by friction at the ground, topography and the vertical distribution of temperature and pressure (Gasch & Twele, 2011b; Stull, 2017; Van Der Tempel, 2006).

As illustrated in Figure 2-6, the ABL consists of three vertical layers. The lowest layer is laminar in nature, only a few millimeters thick, which is not particularly relevant to the wind energy industry. Above it lies the **Prandtl layer**, or surface layer, which extends up to 100 meters. This layer is dominated by turbulent forces, resulting in significant wind shear. The third layer is the **Ekman layer**, where the Coriolis force affects wind direction with increasing height (Bilal, 2016). Above the atmospheric boundary layer, the geostrophic winds are not influenced by the friction at the ground. The height of the ABL can vary widely depending on ground roughness, vertical temperature profile and wind speed. For instance, on a clear night with gentle winds, the ABL may be low as 100 meters, while strong solar irradiance on a warm summer day can extend it up to 2000 meters (Gasch & Twele, 2011b).

The **Prandtl layer** is meteorologically defined as the layer where the turbulent vertical fluxes of momentum, heat, and moisture deviate less than 10% from their surface values, and where the effect of the Coriolis force is negligible (Stefan, 2018b). Typically, the layer accounts for only 10% of the atmospheric boundary layer’s height. The height of the Prandtl layer also varies with the vertical temperature profile. Most wind turbines operate within the Prandtl layer, and the extractable energy, as well as the loads on wind turbines, depend significantly on the properties and intensity of the air mass within this layer (Gasch & Twele, 2011b).

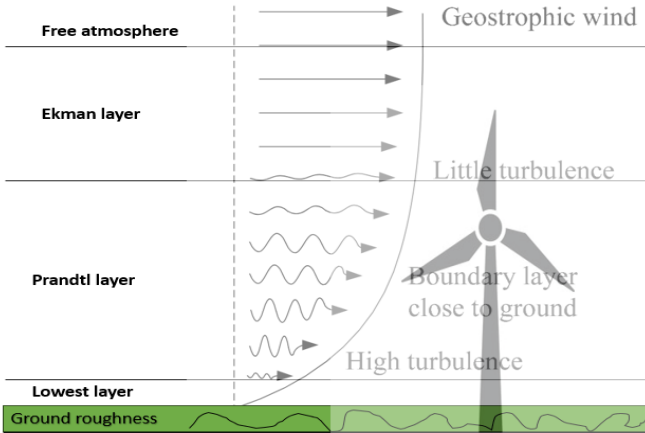


Figure 2-6: Atmospheric boundary layer (ABL) schemes.

Wind shear typically influences wind resource assessment and the design of wind turbines. The representation of wind shear for wind resource assessment can be quite complex and dependent on factors such as atmospheric stability, surface roughness, nature of terrain, wind speed, height above ground and the vertical temperature profile (Gasch & Twele, 2011b; Ray et al., 2006). Understanding the impact of wind shear in the wind energy industry is essential, as it affects power availability at different wind turbine hub heights and influences the cyclic loading on turbine blades caused by variations in the wind field’s vertical direction (Manwell et al., 2010b; Ray et al., 2006). Also, the knowledge of the wind shear’s shape is important for determining the energy yield of a wind turbine.

The use of kite anemometers mounted on meteorological towers (met towers) is an established technique to accurately obtain wind shear profiles on a proposed site. Other techniques, such as remote sensing devices (LiDAR and SODAR) and radiosondes, have gained prominence in the industry. Their main purpose is to measure wind speeds at various turbine hub heights, typically ranging from 60m to 100m. When measurements from lower met tower heights are not close to turbine hub heights, wind shear models can be used to extrapolate wind speeds to desired/target hub height (Ray et al., 2006).

The aforementioned wind shear models, the logarithmic profile (log law) and power law profile, are mathematically derived to describe the shear effect on the mean wind speed at a particular height (Van Der Tempel, 2006).

The log law originates from the principles of boundary layer flow in fluid mechanics and atmospheric research. It is expressed below in Equation 2.3:

$$\frac{U(z)}{U(z_r)} = \frac{\ln(\frac{z}{z_o})}{\ln(\frac{z_{ref}}{z_o})} \tag{2.3}$$

$U(z)$	mean wind speed at target height z	[m/s]
$U(z_{ref})$	mean wind speed at reference height z_{ref}	[m/s]
z_{ref}	reference height	[m]
z	target height	[m]
z_o	surface roughness length	[m]

where z and z_{ref} are the target and reference heights, respectively. $U(z)$ and $U(z_{ref})$ represent the mean wind speed at target height z and the mean wind speed at reference height z_{ref} , and z_0 is the surface roughness length (Manwell et al., 2010b; Ray et al., 2006).

Assuming a smooth surface, the log law can be expressed as shown in Equation 2.4:

$$U(z) = \frac{U^*}{k} \ln \left(\frac{z}{z_0} \right) \tag{2.4}$$

$U(z)$	mean wind speed at target height z	[m/s]
U^*	friction velocity	[m/s]
k	Von Karman's constant	[-]
z	target height	[m]
z_0	surface roughness length	[m]

In this equation, U^* represents the friction velocity, k is Von Karman's constant which equals 0.4, and z_0 is the surface roughness length characterizing the roughness of the ground terrain (Manwell et al., 2010b). The surface roughness length z_0 is the parameter used to represent shear and the height above ground level where the wind speed is theoretically zero. The surface roughness length tends to vary according to the type of terrain. Table 2-1 shows some approximate surface roughness lengths for different terrain types.

Table 2-1 – Approximate surface roughness length for different terrain types (Saheb et al., 2014).

Terrain Description	Surface Roughness Length z_0 [m]
Very smooth, ice or mud	0.00001
Calm open sea	0.0002
Blown sea	0.0005
Snow surface	0.003
Lawn grass	0.008
Rough pasture	0.01
Fallow field	0.03
Crops	0.05
Few Trees	0.10
Many trees, few buildings	0.25
Forest and woodlands	0.50
Suburbs	1.50
City center, tall buildings	3.00

The power law represents a simple model for the vertical wind speed profile. It can be empirically developed, and its basic form is in Equation 2.5:

$$\frac{U(z)}{U(z_{ref})} = \left(\frac{z}{z_{ref}}\right)^\alpha \tag{2.5}$$

The equation variables such as $U(z)$, $U(z_{ref})$, z , and z_{ref} remain the same as defined earlier, with α representing the power law exponent. Based on empirical results, α is commonly taken as $1/7$, indicating agreement between wind profiles and flow over flat terrain (Manwell et al., 2010b).

Research has shown that empirical relationships for the power law exponent α depend on various parameters, including wind speed, surface roughness length, time of day, season, elevation, temperature, nature of terrain, location and numerous thermal and mechanical mixing parameters (Manwell et al., 2010b; Ray et al., 2006; Van Der Tempel, 2006; Wei, 2010). The power law exponent tends to be lower during the daytime and higher at night. Table 2-2 shows the different power law exponent values for various types of terrain (Bechrakis & Sparis, 2000).

Table 2-2 – Power law exponent values for different types of terrain (Bechrakis & Sparis, 2000).

Terrain description	Power law exponent, α
Smooth, hard ground, lake or ocean	0.10
Short grass on untilled ground	0.14
Level country with foot-high grass, occasional tree	0.16
Tall row crops, hedges, a few trees	0.20
Many trees and occasional buildings	0.22-0.24
Wooded country – small towns and suburbs	0.28-0.30
Urban areas with tall buildings	0.40

The values $U(z)$, $U(z_{ref})$, z , and z_{ref} for the variables in the logarithmic law and power law wind shear models can be obtained from typical met tower data measurements. However, parameters z_o and α must be determined empirically. It's important to note that while wind shear models provide valuable insights, they may not perfectly represent reality and thus many not yield accurate predictions of wind speeds at hub height (Manwell et al., 2010b; Ray et al., 2006).

2.1.4 Atmospheric stability

Atmospheric stability significantly influences the vertical wind profile, also known as wind shear. Understanding the behavior of an air mass as it moves upward and downward is crucial to grasping the concept of atmospheric stability. An air mass is defined as a body of air with a consistent number of molecules acting as a cohesive unit. The temperature within an air mass is generally uniform, as there is minimal or no heat exchange with the surrounding air (Bilal, 2016). While an air mass can expand and contract, it remains intact without breaking apart. The space occupied by the molecules within the air mass determines the density of air. The temperature and pressure within the air mass are directly related to the average speed of molecules and the rate at which they collide with the boundaries of the air mass (Ahrens, 2019).

The rate at which air temperature changes with altitude or height is known as the **lapse rate**. When an air parcel ascends to a lower-pressure environment, its volume increases, leading to a reduction in temperature because the heat is spread over a larger volume. This process, which involves no heat exchange with the surrounding environment, is termed an **adiabatic process**. The vertical displacement of air influences the adiabatic temperature change. Near the earth's surface, most temperature changes are **non-adiabatic** due to energy transfer from the surface and the tendency of air mixing, which modifies its characteristics through lateral movement and turbulence (Barry & Chorley, 2009).

The stability of air is determined by comparing the temperature of a rising air parcel to that of its surroundings. The Moist Adiabatic Lapse Rate (MALR) is the rate of temperature change when a saturated air parcel containing water droplets rises or sinks. The MALR varies based on the amount of cooling and warming, with a common value used in the scientific community being approximately 6°C per 1000 meters (Ahrens, 2019). The Dry Adiabatic Lapse Rate (DALR) applies to the upward movement of dry air where no condensation occurs. As the air mass expands, its temperature decreases at a constant rate of 9.8°C per kilometer (Barry & Chorley, 2009; Wallace & Hobbs, 2006b). The Environment Lapse Rate (ELR) results from complex meteorological factor and represents the actual temperature decrease with height. Unlike adiabatic lapse rates, ELR is not a fixed rate and can vary based on the local vertical profile of air temperature (Barry & Chorley, 2009).

Atmospheric stability can be characterized into three states which are: unstable, stable, and neutral. As illustrated in Figure 2-7, the solid, dotted, and dashed lines represent the vertical wind profiles under neutral, unstable, and stable atmospheric conditions, respectively.

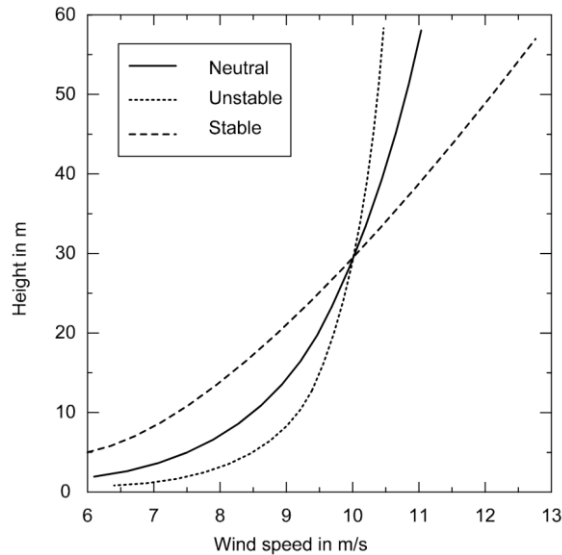


Figure 2-7: Wind profiles in neutral, unstable and stable conditions (Petersen et al., 1997).

Under unstable atmospheric conditions, the air closer to the ground becomes warmer than both its surrounding environment and the air above it. This situation typically occurs during the summer when the sun consistently heats the ground. In such cases, the lapse rate of the surrounding environment is greater than that of the air mass, meaning the rising air mass will be warmer than its surroundings. This difference creates strong vertical mass transfer with increased turbulence. As vertical mixing intensifies under unstable conditions, it results in a smaller gradient of wind speed with increasing altitude (Gasch & Twele, 2011b).

During the stable atmospheric conditions, the rising air mass is colder and denser than its surroundings, causing it to sink back to its original level (Ahrens, 2019). This situation typically occurs during the winter season when the ground cools down, increasing the air density near the surface. Once the air mass is stable, there is minimal vertical mass transfer and suppressed turbulence. Stable atmospheric conditions usually result in high wind shear (Gasch & Twele, 2011b).

In neutral atmospheric stability, the Prandtl layer (surface layer) is neither heated nor cooled. The lapse rate of the air mass is the same as that of the surrounding environment. Consequently,

the vertical displacement of the air mass is neither encouraged nor discouraged. This condition typically occurs at high wind speeds and when there is sufficient cloud cover, preventing strong heating or cooling of the Earth's surface (Bilal, 2016). In such cases, the vertical wind profile depends solely on surface friction rather than thermal mixing in the atmosphere (Gasch & Twele, 2011b).

2.1.5 Atmospheric motions

Wind is a three-dimensional vector, represented as (u, v, w) . The ‘ u ’ component represents the zonal wind, which is the horizontal motion along the east-west axis. A positive value of ‘ u ’ indicates wind blowing from west to east, while a negative value indicates wind blowing from east to west. The ‘ v ’ component represents the meridional wind, which is the horizontal motion along the north-south axis. A positive value of ‘ v ’ indicates wind blowing northward, while a negative value indicates wind blowing southward. The ‘ w ’ component represents the vertical wind, which is the motion along the vertical axis. A positive value of ‘ w ’ indicates upward movement, while a negative value indicates downward movement. These wind components, u , v , and w , correspond to motion in the local Cartesian coordinates in the x , y , and z directions, respectively (Stull, 2017).

The u and v components of wind are often depicted in polar coordinates and used to calculate wind speed ($ws [ms^{-1}]$), and wind direction ($wd [^\circ]$). When averaging ws and wd , it is necessary to transform these values to vector coordinates first. After this transformation, you perform averaging on the vectors (\bar{u}, \bar{v}) , and then transform the averaged vector components back to ws and wd using the equations below (Christiane, 2024). In meteorology, wind direction, wd is defined as the angle where the wind is coming from, hence the use of “–” in Equation 2.6a,b,d. The use of u and v in equation 2.6d might need to be switched around, depending on the used software.

$$u = -ws \cdot \sin (wd) \quad (2.6a)$$

$$v = -ws \cdot \cos (wd) \quad (2.6b)$$

$$ws = \sqrt{u^2 + v^2} \quad (2.6c)$$

$$wd = \frac{180}{\pi} \cdot \text{atan2}(u, v) + 180 \quad (2.6d)$$

2.2 Complex terrain

A complex terrain can be referred to as landforms having varied elevations and features such as steep mountains, valleys, forests, fjords, and urban areas. The Earth’s rotation and land topography, including complex terrain, are key factors that influence wind direction. Consequently, more wind turbines are being sited away from flat regions to complex terrains. Elevated positions like hilltops close to the coasts are common locations for wind turbines in these areas, as they offer more consistent and stronger wind flows (Stefan, 2018c).

Assessing wind resources in complex terrains is often challenging. Global datasets or wind atlases typically offer limited or no useful results. Instead, analytical or numerical weather prediction (NWP) mesoscale models have proven to be effective methods that offer an approximation of the actual wind resources within complex terrain (Solbakken & Birkelund, 2018; Stefan, 2018c). However, it is important to note these models are only virtual approximations of the real atmosphere because of the simplification of terrain characteristics and physical processes (Carvalho et al., 2013).

The illustrations in Figure 2-8 depict topographic features of complex terrain, as defined in articles by (Bitsuamlak et al., 2004) and (Abdi & Bitsuamlak, 2014). In the article by (Abdi & Bitsuamlak, 2014), these features were used as cases in the numerical evaluation of wind flow over various topographies.

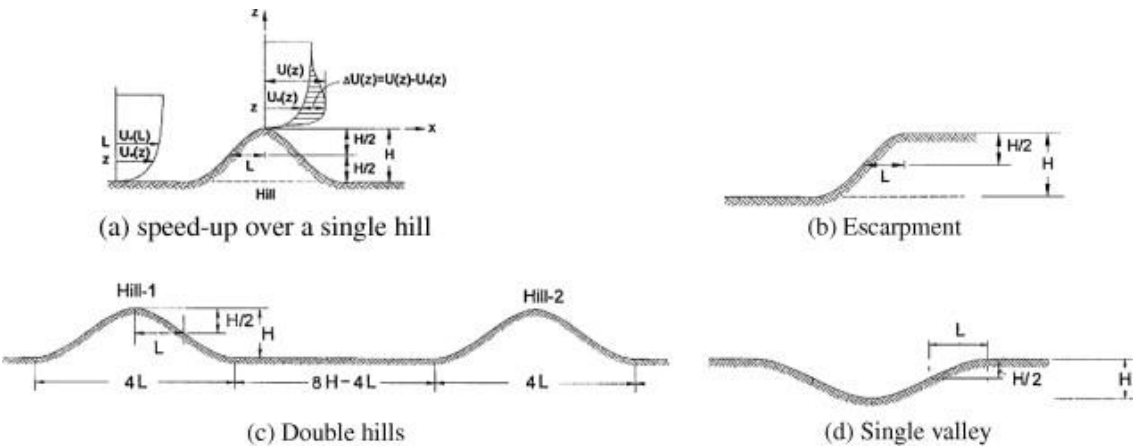


Figure 2-8: Cases of complex terrain features (Abdi & Bitsuamlak, 2014).

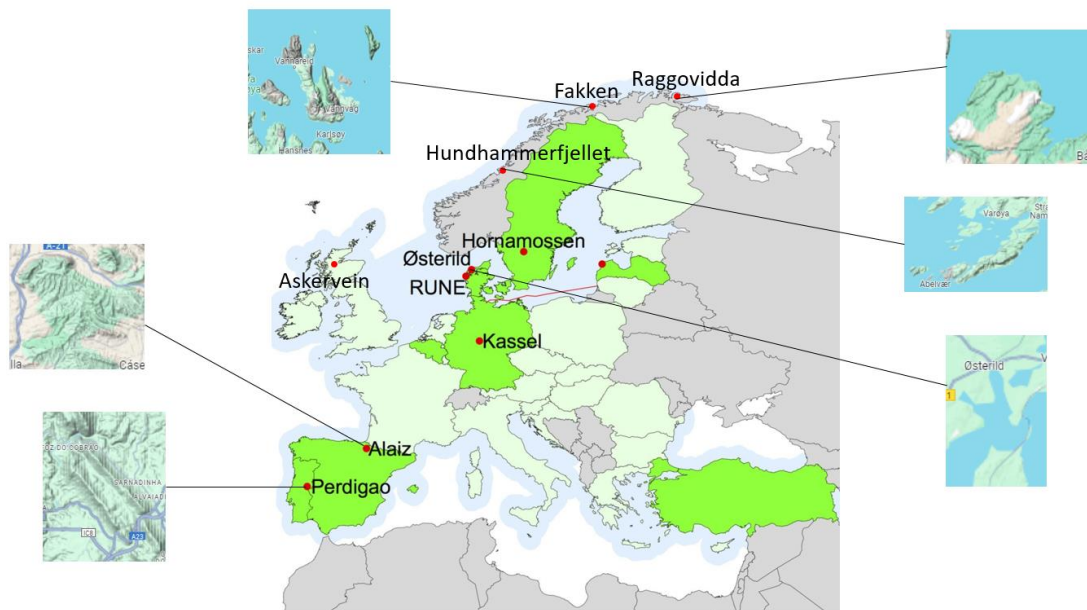


Figure 2-9: Complex terrains showing topography and elevation features.

In an article by (Mann et al., 2017), a series of experiments were conducted in various locations across Europe characterized as complex terrains. These locations have been zoomed in on, as seen in Figure 2-9, to show distinct topography and elevation features. The focus of these experiments was on wind turbines, specifically examining mean flow and turbulence at heights between 40 and 300m. Table 2-3 lists the specific elements of the complex terrain and the corresponding names of the locations where the experiments were conducted.

Table 2-3 – European locations where experiments were conducted and their corresponding complex terrain feature.

S/N	Location	Feature of Complex Terrain
1	RUNE	Coast
2	Østerild	Heterogenies surface
3	Perdigao	Parallel ridges
4	Kassel	Gaussian hill (Forest)
5	Hornamossen	Gaussian hill (Forest)
6	Alaiz	Parallel ridges
7	Askervein	Gaussian hill
8	Hundhammerfjellet	Escarpment
9	Fakken	Small hill, high steep mountains and fjords
10	Raggovidda	Flat inland moutain, close to coast

2.3 Wind phenomena in complex terrain

The land topography and elevation play a pivotal role in wind flow formation in complex terrains. Features of complex terrain such as mountain tops, valleys, fjords, and escarpments can accelerate, reduce, or deflect wind flows (Stefan, 2018c). These interactions create unique wind patterns that differ significantly from those over flat terrains.

Various wind phenomena are formed by the interaction with specific complex terrain features. Mountain and valley breezes typically along mountain slopes. Horizontal differential heating or cooling causes a downslope horizontal pressure gradient along the mountain slopes, driving these winds (Anderson et al., 2005; Renfrew & Anderson, 2006). During the day, the valley floors heat up more intensely than the surrounding elevated areas, causing the air with low density to rise and form a gentle upslope wind known as a valley breeze. At night, this process reverses as the temperature drops around the mountain slopes. The surrounding air cools faster, and due to its higher density, gravity directs the air downhill, resulting in a mountain breeze, also referred to as gravity winds. Katabatic (or fall) winds are another wind phenomenon present downslope on a mountain, which are much stronger than mountain breezes. These winds can move at hurricane-like speeds and can very be gusty (Ahrens, 2019; Stefan, 2018c).

The topography around the area of study, “Fakken Wind park” is characterized by large fjords and high mountain ranges that can potentially create complex flow patterns under specific stability and wind circumstances. According to (National, 1992), gap winds and mountain waves are part of the complex flow patterns produced by coastal orography. Gap winds are particularly dominant in mountain ranges, valleys, and fjords. This phenomenon occurs when wind flows through a gap between two topographically confined channels, resulting in a balance between acceleration and the horizontal pressure gradient. Figure 2-10 illustrates this phenomenon. It is understood that the air is compressed at the gap’s entrance causing high pressure, and expands upon reaching the gap’s exit, causing low pressure (Scorer, 1952). The pressure gradient created at the entrance and exit of the gap causes the air to accelerate through the gap. Consequently, the strength or weakness of the pressure gradient determines the acceleration or deceleration of the gap wind (Jackson & Steyn, 1994; Markowski & Richardson, 2011).

The strongest gap winds occur during winter when a strong anticyclone from the Arctic region develops over the interior east of the Coast Mountains. The Arctic air tends to cool and becomes trapped at the surface between the mountain barriers, separated from the warmer air on the coast (Jackson & Steyn, 1994). The situation creates a large pressure gradient at the gap's entrance, resulting in strong gap winds through the valleys. These winds can be extremely cold and are often accompanied by blizzard conditions, with blowing snow particles.

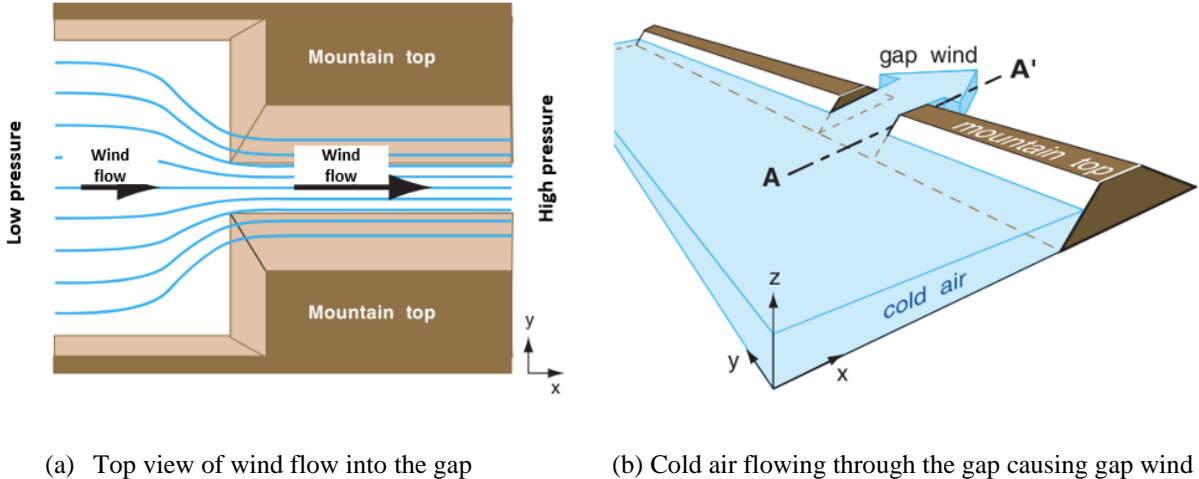


Figure 2-10: Formation of gap winds.

2.4 Wind Energy

Wind is atmospheric air in motion. It is dependent on three factors: volume of air, speed of air, and the mass of air. The velocity of the air in motion defines the magnitude of the wind and is directly proportional to the amount of energy present in the wind (Alexander, 2023). This energy is known as kinetic energy KE and is a function of mass and velocity determined by:

$$KE = \frac{1}{2} mV^2 \tag{2.7}$$

where V is the horizontal wind velocity and m is the mass of the air parcel.

2.4.1 Wind power

Wind power can be defined as the flow rate of kinetic energy. As illustrated in Figure 2-11, wind power quantifies the amount of wind energy in an airflow with velocity V flowing through

an area of interest A per unit time. In other words, wind power is the flux of wind energy through this area.

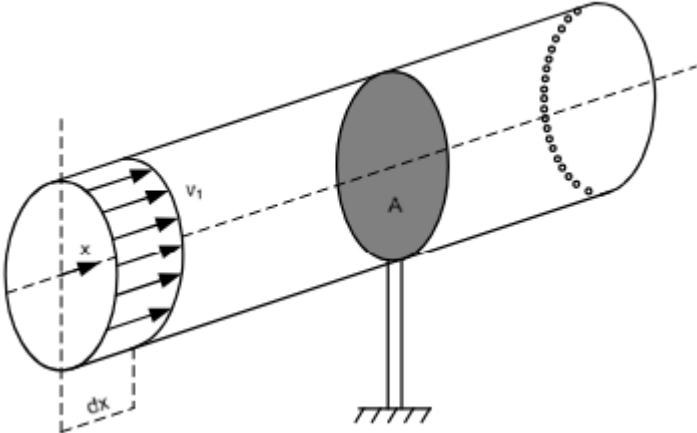


Figure 2-11: Stream tube depicting mass airflow through an area of interest (Gasch & Twele, 2011a).

The volume of air flowing through the area per unit time dt is given by the volume of the cylindrical shape in Figure 2-11 with cross-section area A and length $V \cdot dt$. Thus, the volume is $A \cdot V \cdot dt$. Therefore, the volume flow rate is $A \cdot V$ and the mass flow rate is derived by multiplying the volume flow rate and flow density ρ , given by (Alexander, 2023; Manwell et al., 2010b):

$$\frac{dm}{dt} = \rho \cdot A \cdot V \tag{2.8}$$

Mathematically, wind power can be determined by finding the derivative of kinetic energy with respect to time. By substituting the mass flow rate from Eq. 2.8 into the equation for the mass of the air parcel in Eq. 2.7, we can determine the equation for wind power in Eq. 2.10.

$$P_w = \frac{dKE}{dt} = \frac{1}{2} \cdot A \cdot \rho \cdot V^2 \frac{dx}{dt} \tag{2.9}$$

$$P_w = \frac{1}{2} \cdot \rho \cdot A \cdot V^3 \tag{2.10}$$

Eq. 2.10 shows a nonlinear relationship between wind speed and wind power, meaning that doubling the wind speed results in an eightfold increase in wind power. It is common practice to normalize ambient wind power by dividing it by the area of interest, leading to a term called

“wind power density (WPD),” which represents the kinetic wind energy flux. Wind energy flux is wind energy flow rate per unit area and is given by:

$$WPD = \frac{P_w}{A} = \frac{1}{2} \cdot \rho \cdot V^3 \quad (2.11)$$

It is important to note that wind power density (WPD) provides a quantitative basis for classifying wind resources independent of wind turbine sizes. WPD is proportional to the air density (typically 1.225 kg/m^3 at sea level) and to the cube of the wind velocity (Manwell et al., 2010b).

2.4.1.1 Power from wind turbines

The actual power production potential of a wind turbine must consider the fluid mechanics of the flow passing through a power-producing rotor, as well as the aerodynamics and efficiency of the rotor/generator combination (Manwell et al., 2010b). A wind turbine converts kinetic energy in the wind into mechanical energy, that turns the generator producing electricity. Wind turbines can be utilized both for onshore and offshore purposes. Although wind turbines are available in a broad range of sizes, the main components of a wind turbine include two or three rotor blades, a nacelle, and a tower (Andrews et al., 2022).

A typical modern wind turbine is placed within a wind park configuration and connected to a utility network (Manwell et al., 2010a). In modern turbines, the method of extracting wind energy uses the basic aerodynamics principle of lift, like the wings of an airplane. When a wind turbine encounters a wind flow, there is a low pressure on the upper side of the blade, causing the rotor to turn. This is called lift; the force of this lift is stronger than the force of the wind against the front side of the blade, which causes drag. Electricity is produced as the combination of the lift and drag causes the rotor to turn, leading to the rotation of the generator (Letcher, 2023).

A wind turbine extracts energy by reducing the speed of the passing wind. A theoretically 100% efficient wind turbine would stop the wind flow completely after contact. However, not all power from the wind can be captured and converted into electricity. The fraction of wind power that can be captured by the wind turbine is referred to as power coefficient C_p (Alexander, 2023).

The power coefficient C_p is the ratio of power extracted by the turbine P_t to the total wind power P_w and is given by:

$$C_p = \frac{P_t}{P_w} \quad (2.12)$$

The power extracted by the turbine P_t will always be smaller than P_w and can be rewritten as:

$$P_t = \frac{1}{2} \cdot \rho \cdot A \cdot V^3 C_p = P_w C_p \quad (2.13)$$

(Betz, 1926) and (Lanchester, 1915) discovered that the original upstream wind velocity v_1 is reduced by a cubic factor in the downstream wind velocity v_3 . Therefore, the theoretical maximum power extractable can be given by:

$$P_{Betz} = \frac{1}{2} \cdot \rho \cdot A \cdot V^3 C_{p,Betz} \quad (2.14)$$

with the maximum power coefficient $C_{p,Betz} = 16/27 = 0.59$ (59%), known as the **Betz Limit** (Gasch & Twele, 2011a; Huleihil & Mazor, 2012). This means that even in the best case of power extraction, without aerodynamic and mechanical losses, only 59% of the wind power can be extracted. Wind power production will always be affected by turbine variables, the swept area of the turbine, the capacity coefficient, and atmospheric variables.

2.4.1.2 Power curve

A power curve describes the relationship between wind speed and the power output of a wind turbine (Jing & Ergin, 2023). Figure 2-12 shows a typical power curve of a wind turbine, demonstrating the non-linear relationship between wind speed and generated wind power output.

As illustrated in Figure 2-12, at low wind speeds (< 4 m/s) the wind doesn't apply enough torque to generate electricity. The cut-in speed is the starting point of the curve and represents the minimum wind speed required for the rotor of the wind turbine to turn and start generating electricity. The generated wind power output increases with the cube of the wind speed, reaching a maximum value known as the rated power (Jing & Ergin, 2023). The rated power output is usually obtained when the rotor reaches the maximum speed allowed to turn. At this point, a brake mechanism brings the rotor to a standstill to prevent damage to the blades and

turbine. The cut-out wind speed is the end of the curve, and from Figure 2-12, this is around 25 m/s.

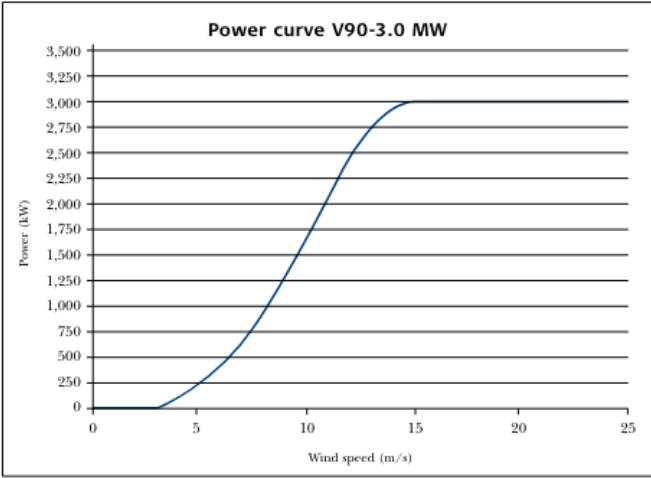


Figure 2-12: Power curve of a Vestas V90-3.0 turbine (Vestas, 2007).

Wind turbine manufacturers determine the measured power curve from simultaneous measurements of the wind speed at hub height and the produced wind power output. The power curve is essential for wind resource assessment and is used to estimate the energy production of a wind turbine over a range of wind speeds. Additionally, power curves are vital in the planning and erection process of wind turbines and are part of the services provided by the turbine manufacturer (Gasch & Twele, 2011b).

The Vestas V90 3MW turbines are currently in use at the Fakken wind-park, and their power curve is shown in Figure 2-12. This turbine has a cut-in speed of 4 m/s, a rated power of 3MW achieved at a wind speed of 16 m/s, and a cut-off wind speed of 25 m/s. In the newly expanded area (Fakken 2), the Vestas V150 6MW turbine is planned for utilization. This turbine is expected to have a cut-in speed of 3m/s, a rated power of 6MW, and a cut-off speed of 25 m/s.

2.4.2 Wind turbine and efficiency

Efficiency is defined as the ratio between the amount of net work done w_{net} and the input energy q_{in} to a device. The efficiency of a wind turbine can be defined as the ratio between the derived power P_{out} and the rate of energy flowing into the wind turbine P_{in} (Huleihil & Mazor, 2012). The efficiency based on this definition aligns with the Betz limit. The efficiency of a power generating wind turbine is given by:

$$\eta = \frac{W_{net}}{q_{in}} = \frac{P_{out}}{P_{in}} \quad (2.15)$$

Another metric to consider in wind turbine power efficiency is the term known as the **Capacity Factor** (CF), which quantifies the fraction of the installed generating capacity that actually generates power (Alexander, 2023). In the terms of a wind turbine, the capacity factor is the ratio of the actual generated energy from the turbine to the energy that could potentially be generated from the wind turbine under ideal environmental conditions. It is mathematically defined as:

$$CF = \frac{E_{actual}}{E_{ideal}} = \frac{time \cdot \bar{P}}{time \cdot P_N} = \frac{\bar{P}}{P_N} \quad (2.16)$$

Considering that energy is the product of its time rate, the energy ratio $\frac{E_{actual}}{E_{ideal}}$ equals the average power \bar{P} and the nominal power P_N of the wind turbine. The nominal power of a single wind turbine is equal to the maximum power that can be generated under ideal wind conditions.

When estimating the efficiency of a wind turbine, different parts of the turbine need to be highlighted. Most of the efficiency terms discussed so far center around the kinetic energy efficiency η_{KE} . However, other factors affecting wind turbine efficiency include: the mechanical efficiency η_{ME} due to mechanical friction, the electricity conversion efficiency η_{CON} , and the blockage efficiency η_{BL} which accounts for the amount of air blocked by turbine blades (Huleihil & Mazor, 2012). A net turbine efficiency can be further defined as:

$$\eta_{net} = \eta_{BL} \cdot \eta_{CON} \cdot \eta_{ME} \cdot \eta_{KE} \quad (2.17)$$

2.4.3 Wake losses

The occurrence of wake losses in wind parks is a well-known phenomenon. A wake occurs when the first turbine or row of turbines extract energy from the wind upstream. As a result, the wind leaving the turbine will have lower energy content, reduced speed, and increased turbulence compared to the wind upstream of the turbine (González-Longatt et al., 2012; Koch et al., 2005). There is always an inevitable loss of power output from each turbine affected by wakes from nearby and distant turbines. Despite being a well-documented, power losses due to turbine wakes can be difficult to predict accurately because of the temporal and spatial

variability of wind speed, wind direction, turbulence, and atmospheric stability (Barthelmie & Jensen, 2010).

In Figure 2-13, there are three distinct descriptions of wind turbine wakes from different wind campaigns. The left image shows the condensation plumes from the Horns Rev 2 offshore wind park, visible to the human eye. The middle image shows wind speed deficits measured by radar, and the right image shows modeled wind speed deficits on an offshore wind park. As established, the two main wake effects are: wind speed reduction, leading to a reduction in energy production of the wind park, and an increase in the wind turbulence, potentially increasing the dynamic mechanical load on the downwind turbines (González-Longatt et al., 2012).

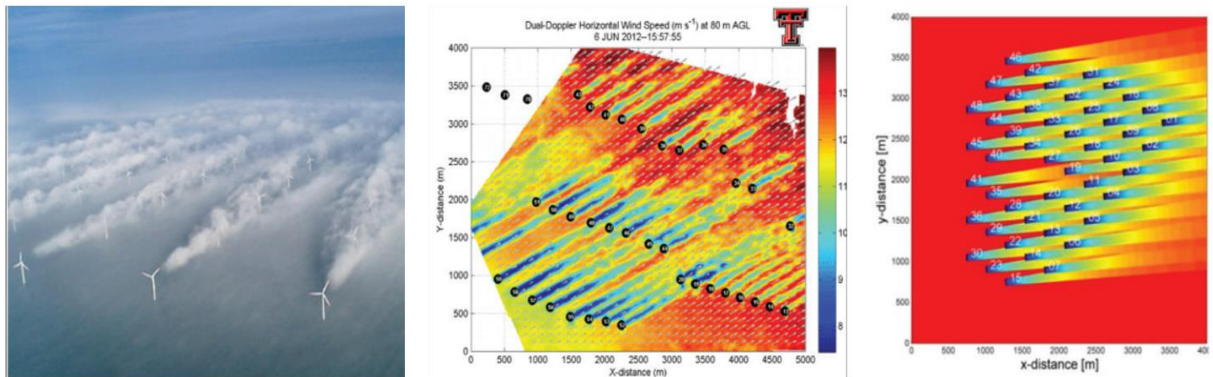


Figure 2-13: Three distinct descriptions of wind turbine wakes. Left: Condensation plumes produced by turbulence within turbine wakes in the Horns Rev 2 offshore wind park (Hasager et al., 2017). Middle: Wind speed deficits within turbine wakes from a complex wind field measured with a Doppler Ka-band radar (Texas, 2014). Right: Simulation of wind speed deficits for the Lillgrund offshore wind project using the Jensen model with a wake decay constant of 0.04 (Smith et al., 2012).

It is essential to describe a wake accurately before considering its effects in the design of a wind park. Numerous numerical models with varying complexities have been developed to describe wake accurately. Some of these models include Ainslie’s model (Ainslie, 1988), Frandsen’s model (Frandsen et al., 2006), the Mosaic Tile model (Rathmann et al., 2007), and the Jensen model (Jensen, 1983). These wake models should be straightforward, dependent on relatively few measurements, and economically feasible in terms of computing power (Barthelmie et al., 2009). In an article by (Ying & MD, 2005) it was suggested that to reduce wake losses in wind parks, wind turbines should be spaced 5-9 rotor diameters apart in the prevailing wind direction and 3-5 rotor diameters apart in the direction perpendicular to the prevailing wind.

2.4.4 Micro-siting

Micro-siting is the process of utilizing wind resource assessment tools, CFD software, and Geographic Information Systems (GIS) to optimize the placement of wind turbines within a selected area. This optimization aims to maximize energy production and reduce turbine wake effects and turbulence (Manwell et al., 2010c). Micro-siting is a crucial step when planning a wind park. Other factors to consider include the wind resource, land availability, environmental conditions, the possibility of connection to the electrical transmission system, and proximity to access roads (González et al., 2014). One objective of micro-siting is to locate wind turbines in the wind park to maximize annual energy production (AEP) and potentially yield a significant return on investment (ROI) for the wind park owners.

Several commercial software packages aid in micro-siting by assessing wind resources on a microscale level. The most popular of these is “WAsP,” which is considered the industry standard for wind resource assessment using a microscale flow analysis (González et al., 2014). Other software includes “WindSim,” which assesses the wind resource using a CFD model based on a 3D Reynolds-averaged Navier-Stokes (RANS) solver to pinpoint less turbulent locations with strong wind speed conditions, particularly in complex terrain (WindSim, 2024) and “Metodyn,” which estimates wind resources over a plot using CFD simulations and integrate results from other mesoscale analysis data. Additional software such as “Windfarmer,” “WindPro,” and “OpenWind” optimize the wind turbine layout of wind parks to maximise ROI and minimize the cost of energy production (González et al., 2014).

The Katic model is the widely accepted in the wind energy industry for micro-siting and is utilized across most software. It is a wake model proposed by (Katic et al., 1987) for the evaluating a wind park’s energy yield taking into account the wake effect.

Effective micro-siting depends on a combination of detailed wind resource information from a specific site and typically involves using CFD models to predict the detailed flow field in the wind park (Manwell et al., 2010b). The output results are usually combined with another model that predicts the power production output of the wind park.

2.5 Wind data visualization

It is crucial in the wind energy industry to interpret and analyze complex wind patterns and trends effectively. Visualization techniques play a key role in transforming raw wind data, often presented in numerical or otherwise incomprehensible forms, into actionable insights. These insights are essential for the planning and optimization of wind energy projects. An anemometer is a conventional tool for measuring the strength and speed of the wind (Hakstok & Mihajlović, 2014). In visualizing wind data, wind direction and wind speed are essential factors needed to evaluate wind resources and potential wind power production at a particular wind park site.

These visualization techniques leverage direct (non-statistical) and statistical data analysis methods (Manwell et al., 2010b). Common wind data visualization methods include wind rose diagrams, histogram of wind speeds, and wind speed distribution functions such as Weibull and Rayleigh distributions. These visualizations help wind park stakeholders make informed decisions on turbine placement, performance assessment, and overall wind park efficiency.

2.5.1 Wind roses

A wind rose is an essential tool for evaluating wind resources in a wind park or a specified area, as it indicates the predominant wind direction at a given location. It is a convenient tool for displaying anemometer data (wind speed and direction) for turbine siting analysis. An example of a wind rose is shown in Figure 2-14. The wind rose in Figure 2-14 illustrates its most common form, which consists of different color bands showing the range of wind speeds (Chavan et al., 2017).

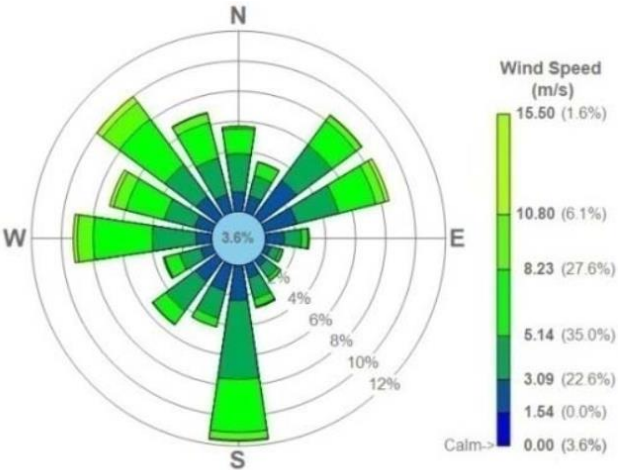


Figure 2-14: Example of a wind rose diagram (Chavan et al., 2017).

The wind rose depicts the occurrence of winds within various directional sectors, with each sector featuring color-coded categories that indicate the frequency of different wind speeds in a particular direction. The frequency in a wind rose is represented by the concentric circles. There are usually calm conditions at the center circle of the wind rose, and the longest lines show the prevailing wind directions (Manwell et al., 2010b). Wind roses are specifically created for a particular area over a period (i.e. annually, seasonally, and monthly) and are divided into 8-16 sectors, one for each direction. There are many variations considered in the construction of a wind rose, primarily including the wind speed ranges, and some indicate other meteorological parameters along with the wind direction (Varma et al., 2013).

A wind rose shares useful information in planning the layout of wind turbines in a wind park, helping to optimize the energy output of wind turbines. It is known that one of the significant factors impacting turbine performance is wake losses. To mitigate substantial wake losses, wind roses offer information about long-term wind patterns that help to strategically position turbines to align with the direction of least wind occurrence.

2.5.2 Histogram of wind speeds

A histogram of wind speed is a crucial tool in wind energy analysis, representing the frequency distribution of wind speeds over a specific period. Figure 2-15 illustrates a typical histogram (bar graph), showing wind speed values plotted on the x-axis and the frequency of each wind speed occurrence on the y-axis. Histograms of wind speeds work with long-term wind data; for example, the histogram below was derived from one year of hourly data, with a mean wind speed of 5.91 m/s and a standard deviation of 2.95 m/s (Manwell et al., 2010b).

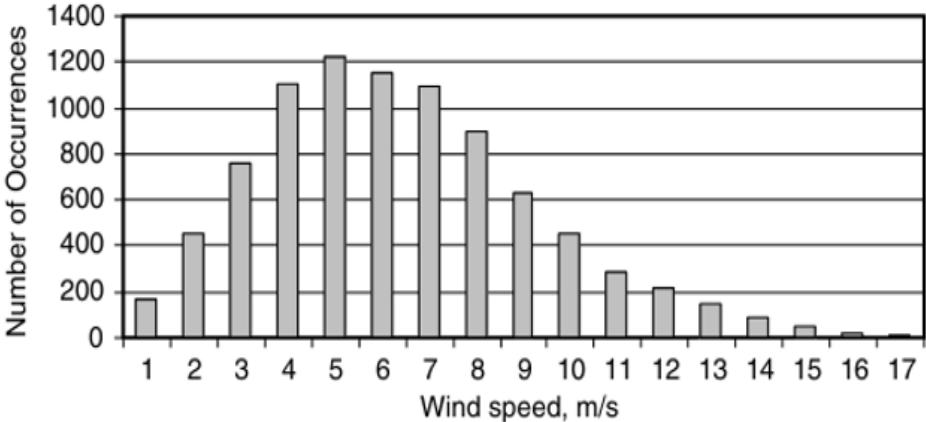


Figure 2-15: Sample of a typical histogram showing wind speed frequencies.
 Page 30 of 81

This form of wind data visualization aids in understanding the variability and distribution of wind speeds at a particular location. It provides a concise way to summarize wind data and determine expected turbine productivity. Wind-park planners utilize histograms to identify wind speed ranges that are most likely to yield the highest energy output, ensuring the strategic placement of turbines.

2.5.3 Weibull distribution function

The number of occurrences of wind speeds can be described by the probability density function $p(U)$ of wind speed. This function represents the likelihood that the wind speed has a particular value. From past studies, wind speeds are more likely to be close to the mean value or below it (Manwell et al., 2010b).

A Weibull distribution function is one of the two most common probability distribution functions used for wind data analysis. The other common probability distribution function is the Rayleigh distribution function. The Weibull distribution function, named after the Swedish engineer and mathematician Ernst Hjalmar Waloddi Weibull, describes the frequency distribution of wind speed at the low-frequency end ($< 0.01 - 0.001$ Hz) of the spectrum (Stefan, 2018a). It is governed by two parameters: a shape factor k (dimensionless) and a scale factor c (m/s). Both parameters are functions of the mean wind speed \bar{U} and the standard deviation of wind speed σ_U . The Weibull distribution function is given by:

$$F(U) = 1 - \exp\left[-\left(\frac{U}{c}\right)^k\right] \quad (2.18)$$

Figure 2-16 shows an example of a Weibull distribution function for different values of the shape factor k . As illustrated, an increase in the value of k creates a curve with a sharper peak, indicating less wind speed variation. The Weibull distribution function is essential in describing the histogram of wind speeds, as the frequency distribution of wind speeds often aligns well with the Weibull distribution function. Overall, the Weibull distribution function, along with the wind turbine power curve, helps greatly in the planning phase of a wind park by estimating the annual energy production (Giorgos, 2022).

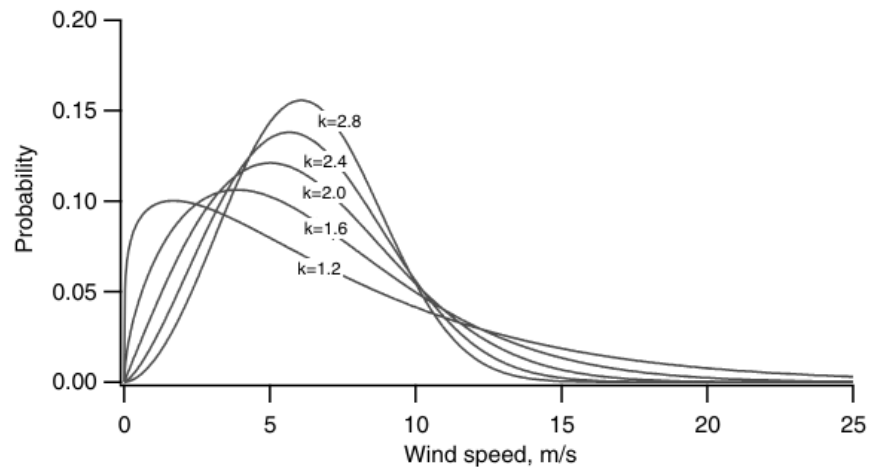


Figure 2-16: Example of a Weibull distribution function for mean wind speed \bar{U} of 6 m/s (Manwell et al., 2010b).

2.6 Evaluating models

Statistical metrics can be used to evaluate the accuracy of models compared to the observed values. These metrics indicate the closeness of models to estimating the actual values. These evaluations utilize time series: the observed values y_i and the simulated values \hat{y}_i , where i represents the data points ($i = 1, 2, \dots, N$)

There are numerous statistical measuring methodologies which compare the deviation between the model and observed values. These methodologies are:

1. **Root Mean Square Error (RMSE)** is a standard statistical method frequently used for evaluating model performance in various studies. RMSE is particularly effective for estimating the variance and dispersion between predicted models and observed values (Solbakken & Birkelund, 2018). One key advantage of RMSE is its ability to penalize large errors more heavily, making it a suitable metric in scenarios where larger deviations are especially critical to minimize.

$$RMSE = \sqrt{\frac{1}{N} \sum_{i=1}^N (\hat{y}_i - y_i)^2} \quad (2.19)$$

2. **Bias** is the deviation between the observation mean and the estimated mean. It is given by:

$$Bias = \frac{1}{N} \sum_{i=1}^N (\hat{y}_i - y_i) \quad (2.20)$$

3. **Mean Absolute Error (MAE)** is the deviation between a corresponding observation and estimation. It is given by:

$$MAE = \frac{1}{N} \sum_{i=1}^N |\hat{y}_i - y_i| \quad (2.21)$$

4. **Mean Absolute Percentage Error (MAPE)** is a metric used to measure the average deviation of predicted values from actual values, expressed as a percentage (Khair et al., 2017).

$$MAPE = \frac{1}{N} \sum_{i=1}^N \left| \frac{\hat{y}_i - y_i}{y_i} \right| * 100 \quad (2.22)$$

According to (Solbakken & Birkelund, 2018), the RMSE, MAE, and Bias express the average model estimation error. They range from 0 to infinity while the RMSE and MAE are indifferent of the errors.

2.7 Light Detection and Ranging (LiDAR)

The rapid development of LiDAR measurement techniques began with the invention of the laser in 1960 by Theodore Maiman (Maiman, 1960) and the giant-pulse or Q-switched laser in 1962 (McClung & Hellwarth, 1962). According to (Ulla, 2005), the five established LiDAR techniques are elastic-backscatter LiDAR, Raman LiDAR, differential-absorption LiDAR, resonance fluorescence LiDAR, and Doppler LiDAR.

The elastic-backscatter LiDAR is a classic form of LiDAR. In its simplest form, it uses a laser emitting a single wavelength and a detector measuring the radiation elastically backscattered from atmospheric molecules and particles. The Raman LiDAR measures water vapor and atmospheric temperature profiles (Behrendt et al., 2002). The differential-absorption LiDAR (DIAL) offers the ability to detect atmospheric gases with high sensitivity using single absorption lines (Ulla, 2005). The resonance fluorescence LiDAR applies resonance scattering within the mesopause region (80 – 110km height) in the presence of layers containing metallic atoms and ions. The Doppler LiDAR is an emerging method for wind sampling (Reitebuch & Hardesty, 2021).

Doppler wind LiDAR, being a remote sensing technique, allows for the observation of wind speed without interrupting the atmospheric flow. Doppler wind LiDAR observations are used to study atmospheric flow on various temporal and spatial scales, covering a substantial vertical and spatial extent of the atmospheric boundary layer. The relevance of the Doppler wind LiDAR in the wind energy industry has accelerated the development of small, commercially available wind LiDAR systems. Doppler wind LiDARs are typically operated from the ground and are commonly used for wind resource assessment, wind energy site assessment and, turbine wake visualization (Emeis et al., 2008; Hasager et al., 2017; Krutova et al., 2022; Mikkelsen, 2014). They are also used for airport surveillance for low-level wind shear (Shun & Chan, 2008) and aircraft safety and control (Köpp et al., 2004). Additionally, Doppler wind LiDARs have been utilized in the research of atmospheric dynamics in complex terrains (Risan et al., 2018; Zhao et al., 2020) and for turbulence measurement using multiple wind LiDARs (Mann et al., 2009; Sathe & Mann, 2013), with a notable example being the Perdigão campaign documented by (Fernando et al., 2019).

As the name suggests, the Doppler wind LiDAR utilizes the Doppler effect to measure atmospheric wind velocity (Reitebuch & Hardesty, 2021; van Dooren, 2022). The Doppler effect describes the change in frequency or wavelength when the source of a wave and an observer are in relative motion. The emitted light has a wavelength, λ_0 , and the frequency is $f_0 = c/\lambda_0$, where c is the speed of light. The relative speed along the line of sight (LOS) is denoted as v , and the observed frequency is given by (Christian, 2005):

$$f = f_0(1 + v/c) \quad (2.19)$$

Using a Doppler wind LiDAR, the Doppler effect occurs twice because the LiDAR both emits (source) and receives (observer) the laser beam. The light wave from the emitting laser source in the wind LiDAR has a frequency, f_0 , which interacts with a moving particle (e.g., aerosol or cloud particle). The moving particle (observer) senses this light wave and then re-emits (source) it with the frequency, f_2 , which is observed again by the wind LiDAR. The Doppler frequency shift, Δf , is given by:

$$\Delta f = f_2 - f_0 = 2 \cdot f_0 \frac{v_p}{c} \quad (2.20)$$

The frequency shift is determined by the speed of the moving particle, v_p , relative to the speed of light, c . Conventional Doppler wind LiDAR usually emit at infrared wavelengths between $1.55 \mu m$ ($f_0 = 193\text{THz}$) and $2.02 \mu m$ ($f_0 = 148\text{THz}$), with corresponding frequency shifts of $\Delta f = 1.29 \text{ MHz}$, or $\Delta f = 0.99 \text{ MHz}$, for $v = 1 \text{ m s}^{-1}$ (Reitebuch & Hardesty, 2021).

As illustrated in the left image in Figure 2-17, the beam from the wind LiDAR interacts with multiple particles within a certain atmospheric volume, each possessing its own velocity. The collective velocities of the particles represent the wind velocity with added small-scale and random (or turbulent) motion.

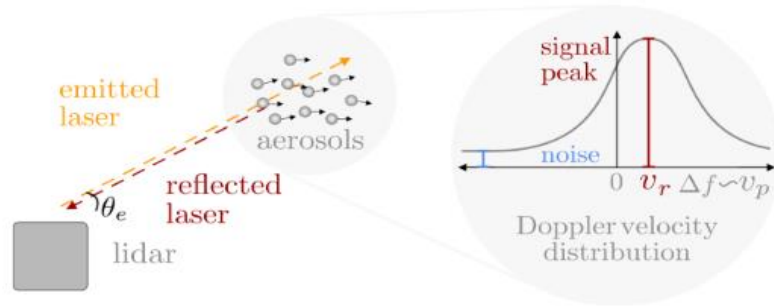


Figure 2-17: Schematic of the Doppler wind LiDAR measurement principle. Left: LiDAR beam interacting with aerosol particles. Right: Idealised distribution of aerosol Doppler velocities over the LiDAR volume based on the frequency shift between emitted and returned laser signal (Christiane, 2024).

The wind LiDAR receives a distribution of Doppler frequency shifts, also known as “Doppler broadening”, in the returning signals for the bulk of air particles. The signal peak, as seen in the right image in Figure 2-17, measures the wind velocity averaged over the measured volume. The width of the Doppler frequency shift distribution (or Doppler velocity distribution) measures the turbulent motion superimposed on the average wind velocity. The peak velocity observed by the LiDAR is the wind velocity projected onto the line-of-sight (LOS) of the LiDAR’s laser.

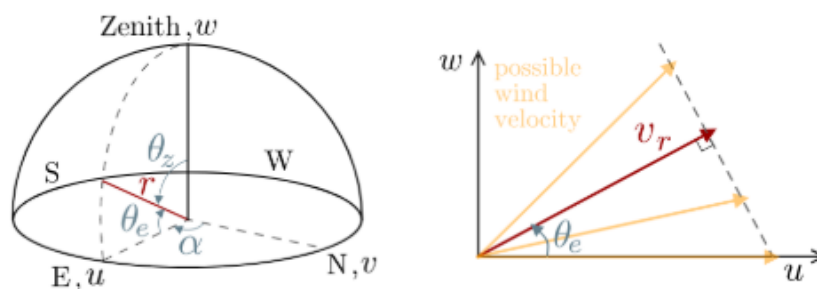


Figure 2-18: Polar coordinates (Left): azimuth angle, α , elevation angle, δ , or zenith angle, θ_z and range, r . Right: Projection of radial velocity in a vertical plane along the horizontal x-axis (u and w). The combinations of u and w along the gray striped line perpendicular to the LiDAR’s beam orientation resulting in radial velocity (Christiane, 2024).

Therefore, v_{LOS} is the line-of-sight (LOS) wind speed measured by the LiDAR. If the air particles (aerosols) at the measurement point are moving towards the observer, v_{LOS} will be positive; if moving away, v_{LOS} will be negative (van Dooren, 2022). The increase and decrease of v_{LOS} affect the frequency in the same manner. The direction of the LOS is usually defined in polar coordinates using the elevation angle, δ , or zenith angle, $\theta_z = |90 - \delta|$, azimuth angle, α , and range, r , as defined in Figure 2-18. The velocity measured along the LOS of the

laser beam is called radial velocity, v_r , and this is connected to the Cartesian wind speed components, u , v , and w as follows:

$$v_r(r, \alpha, \theta_z) = u(r) \sin \alpha \sin \theta_z + v(r) \cos \alpha \sin \theta_z + w(r) \cos \theta_z \quad (2.21a)$$

$$v_r(r, \alpha, \delta) = u(r) \sin \alpha \cos \delta + v(r) \cos \alpha \cos \delta + w(r) \sin \delta \quad (2.21b)$$

The variable “Signal-to-Noise Ratio”, (SNR) or “Carrier-to-Noise Ratio”, (CNR) is derivable from the wind LiDAR observations, based on the velocity peak intensity relative to the noise intensity of the relevant spectral bandwidth, as illustrated in Figure 2-17. The SNR/CNR measures the density of air particles (aerosol, cloud) in the boundary layer and cloud detection. By deploying different wind LiDAR scanning strategies, which will be focused on in the next chapters, all components of the wind vector can be derived, and they are listed in Table 2-4.

Table 2-4: Measured parameters of a Doppler wind LiDAR (Reitebuch & Hardesty, 2021).

Parameter	Description	Unit	Symbol
LOS speed	Wind speed in direction of the laser line-of-sight (LOS) or radial wind speed	[m/s]	v_{LOS}
Wind speed	Magnitude of horizontal wind speed	[m/s]	M
Wind direction	Angle for horizontal wind direction with respect to North, where wind is blowing from	o	θ
Wind velocity components	Components of the wind vector with zonal wind speed (East–West) u , meridional wind speed (North–South) v , vertical wind speed w (up-down)	[m/s]	u, v, w
Signal intensity	Signal intensity of the backscattered signal	arb. u. or dB	I
Signal-to-noise ratio, carrier-to-noise ratio	Ratio of signal intensity (or carrier) to noise intensity for the relevant spectral bandwidth	arb. u. or dB	SNR, CNR

There are two main types of Doppler LiDAR technologies used in the industry today: the pulsed LiDAR and the continuous wave (CW) LiDAR. Most technological advancements have been linked to the long-range pulsed LiDAR systems, as seen in Figure 2-19. Pulsed wind LiDARs can observe radial velocity simultaneously at multiple ranges, maintaining a constant range resolution even with increasing range. However, pulsed wind LiDARs are limited in measuring short distances, typically starting at 50 – 100 meters from the wind LiDAR.

On the other hand, the CW wind LiDAR systems focus on a single range, exhibiting high precision within the first tens of meters, with a range resolution in the order of centimeters. Nevertheless, their range resolution decreases considerably with increasing distance from the LiDAR, and their range is limited to approximately 100 meters. The application of CW wind LiDARs to obtain high precision wind measurements in the lowest range of the wind profile complements the inadequacy of pulsed wind LiDARs to measure short distances.

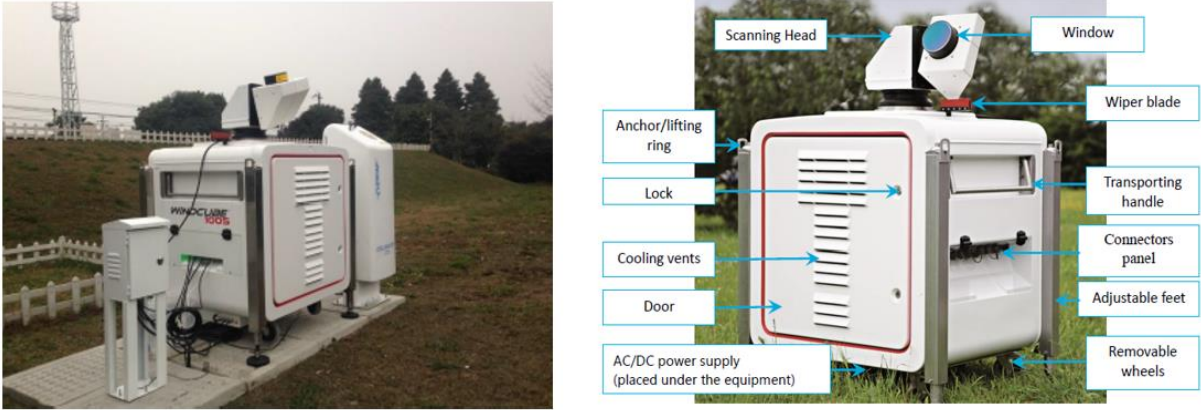


Figure 2-19: External view and features of the Leosphere WindCube100s (WLS100s) scanning LiDAR (Leosphere, 2023).

3 Data and Methods

3.1 Description of Fakken wind park

The area of interest in this thesis is the Fakken wind park, located at coordinates of $70.10^{\circ}N$ and $20.06^{\circ}E$ which around the eastern side of Vannøya in Karlsøy municipality placed in the Northern Norway. The wind park is characterized by its Arctic climate and coastal conditions. In the winter season, there is a contrast in temperatures between the frigid air over land and the warm air over the ocean due to the North Atlantic current. This results in a pressure difference from east to west, with higher pressure over the land and lower pressure over the ocean. In the summer season, the temperature and pressure gradients are often inverted, causing the main wind direction to come from the northeast (NE), while the main wind direction during the winter is southeast (SE) (Svendsen, 1995)

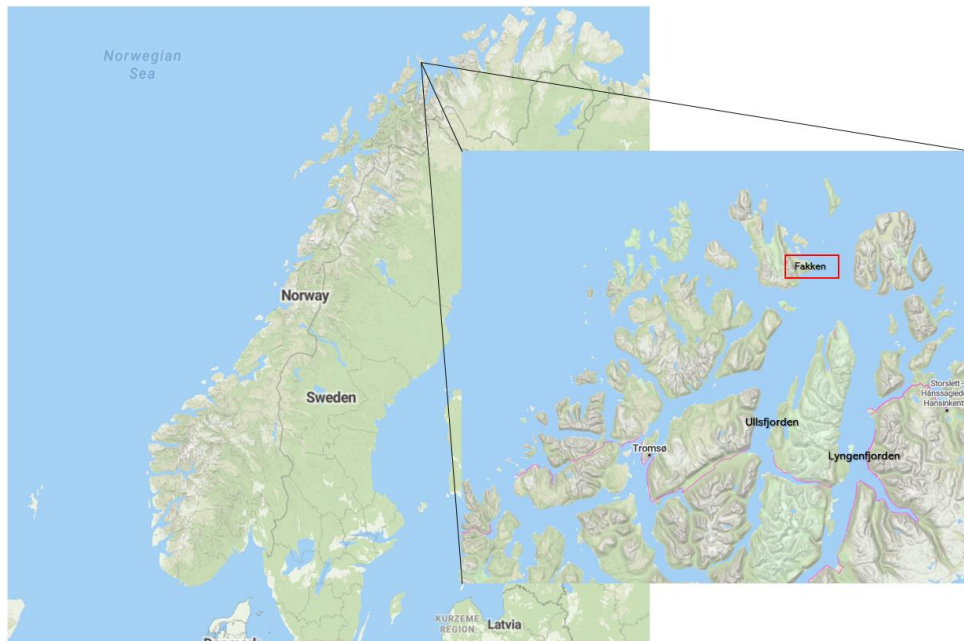


Figure 3-1: Map of the region with the Fakken wind park in red square.

The surrounding terrain influencing the wind resources around Fakken wind park is seen in Figure 3-1. The wind park has relatively flat terrain and is located 40 to 200 meters above sea level. The region features a diverse topography, including multiple mountain ranges. It faces the open ocean to the north, while to the south it is surrounded by landmasses characterized by large fjords and high mountains. As seen in Figure 3-1, Two significant fjords, Ullsfjorden and Lyngenfjorden, are directly south of this region.

This complex and diverse terrain has a substantial impact on the region’s wind resources, allowing for wind phenomena such as gap winds to occur (Solbakken et al., 2021). Figure 3-2 provides more insight into the height of the terrain of the topography surrounding the Fakken wind park. The figure depicts elevations exceeding 1300 meters as white spots, while areas with elevations between 500 and 1000 meters are shown as greenish-brown spots. This figure highlights the significance of elevation differences within Vannøya and its surrounding area, illustrating the complex and varied topography.



Figure 3-2: Terrain height of the topography around Fakken wind park (Norgeskart, 2023).

The Fakken wind park is an established wind park with 18 turbines, each rated at 3 MW, giving a total rated power capacity of 54 MW. Each turbine has a hub height of 80 meters above ground level (a.g.l.) (Troms, 06.11.2023). As illustrated in Figure 3-3, the turbines are sited in two rows to minimize wake losses and maximize energy production from the wind park. The turbines are numbered from 1 to 18 from west to east, including the met mast. The proposed expansion to Fakken II wind park will site the new turbines northwest of the current Fakken I wind park. The highlighted blue area in the left image in Figure 3-4 indicates the new site for Fakken II, which

is expected to have a power output capacity of 66 MW with 11 turbines, each rated at 6 MW and a hub height of 112 meters a.g.l.

The preliminary positions for each wind turbine at Fakken II are labelled with letters (A-K) as illustrated in the right image in Figure 3-4. Troms Kraft, the owners of Fakken I wind park, suggested coordinates for the new 11 turbines, which have been considered in this thesis. In the appendix B section of this thesis, the wind turbine coordinates for both Fakken I and II will be listed in a table for better understanding.

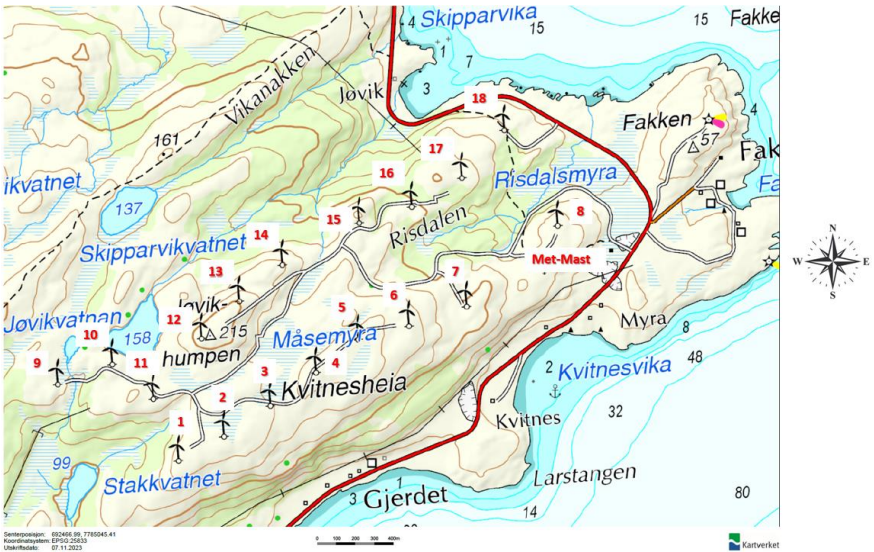


Figure 3-3: Siting of wind turbines in Fakken I



Figure 3-4: Planning for Fakken II. Left: New site location for Fakken II. Right: Proposed siting of new turbines in Fakken II

3.2 LiDAR Setup

The Doppler wind LiDARs used for the measurement campaign at the Fakken wind park were two scanning (WindCube 100s) pulsed long-range Doppler wind LiDARs, manufactured by Leosphere, now owned by Vaisala. The data used in this thesis was obtained after the successful conclusion of the campaign. The two WindCube 100s Doppler wind LiDARs were operational from mid-December 2022 to June 2023, a period characterized by strong chill winds and a high probability of icing (Ahrens, 2019). The two pulsed long-range Doppler wind LiDARs, tagged LiDAR 34 and LiDAR 40, were positioned in Fakken I near two wind turbines tagged WTG10 and WTG15.

LiDAR 34 and LiDAR 40 were levelled and oriented towards the north using nearby hills as hard targets. The turbines were not considered as hard targets due to the movement of the blades. The scanning head for both LiDARs was positioned to face a “fixed” point in the northeast direction, where Fakken II is proposed to be sited. According to the plan shared by Troms Kraft, the fixed point will be the proposed location for setting up the meteorological mast for Fakken II. As shown in Figure 3-5, black pointers indicate the positions of LiDAR 34 and LiDAR 40, while the green pointer marks the fixed point within Fakken II.



Figure 3-5: Placement of LiDAR34, LiDAR40 and Fixed point in Fakken II.

Additionally, the locations of the two LiDARs, the fixed point in Fakken II, and the closest turbines to both the LiDARs and the fixed point are listed in Table 3-1 using various coordinate

systems (Geographical degrees, UTM-zone 34W, and cartesian coordinates). Both LiDAR 34 and LiDAR 40 were configured to operate only in the scanning mode while being governed by different scanning techniques.

Table 3-1: Locations of LiDARs, fixed point in Fakken II, closest turbines to LiDARs and fixed point in various coordinate systems.

Objects	Geographical degrees (Lat/Lon)	UTM-zone 34W (northing/easting)	Northing(m)	Easting(m)
LiDAR 34	70.09752/20.03064	7777041/463173	-516	-1415
LiDAR 40	70.10234/20.06769	7777557/464588	516	1415
Fixed point in Fakken II	70.10550/20.01150	7777943/462460	386	-2128
WTG_10	70.09652/20.03219	7776929/463230	-606	-1358
WTG_15	70.10214/20.06769	7777535/464588	606	1358
Turbine F	70.1055/20.01247	7777942/462497	1013	-733

3.2.1 Scanning LiDAR scan patterns

3.2.1.1 Fixed scan

The simplest scan technique used in the scanning mode of the Doppler wind LiDARs is the “fixed LOS” (Line of Sight). Here, the scanning LiDAR obtains a time series of radial velocity, v_r , while the scanner head is oriented towards a fixed azimuth angle, α , and elevation angle, δ . Each wind LiDAR scans in the fixed LOS mode for the first thirty minutes and last twelve minutes within an hour. The values for the azimuth angle and elevation angle for LiDAR 34 and LiDAR 40 respectively are: $\alpha_{34} = 324^\circ$, $\alpha_{40} = 280^\circ$, $\delta_{34} = 4.75^\circ$, and $\delta_{40} = 3.89^\circ$. Using the elevation angle, the horizontal wind speed at the fixed point in Fakken II can be calculated for each LiDAR. The mathematical formula in Eq.3.1 is applied to calculate the horizontal component, v_h , at the selected range for each LiDAR closest to the fixed point.

$$v_h = \frac{v_{LOS}}{\cos(\delta)} \quad (3.1)$$

The selected range for LiDAR 34 is 1210 meters while the selected range for LiDAR 40 is 2150 meters. This indicates that the laser beam from LiDAR 40 covers more ground than LiDAR 34. In the calculation of the horizontal component, it is assumed that the vertical wind speed is negligible because the vertical component w adds to the v_{LOS} with the sine of the elevation angle. Therefore, for elevation angles less than 10° , there will be low fluctuations to be

considered in the calculation of horizontal component. The next step is retrieving the horizontal wind speed components u and v . The mathematical formula in Eq.3.2 is calculated from the horizontally projected radial speeds of both LiDARs using the linear system (Schneemann et al., 2014):

$$\begin{pmatrix} v_{h34} \\ v_{h40} \end{pmatrix} = \begin{pmatrix} \sin(\alpha_{34}) & \cos(\alpha_{34}) \\ \sin(\alpha_{40}) & \cos(\alpha_{40}) \end{pmatrix} \cdot \begin{pmatrix} u \\ v \end{pmatrix} \quad (3.2)$$

Eq.3.3 yields mathematical formulas that calculate the u and v components

$$u = \frac{v_{h34} \cos(\alpha_{40}) - v_{h40} \cos(\alpha_{34})}{\sin(\delta_{34} - \delta_{40})} \quad \text{and} \quad v = \frac{v_{h40} \sin(\alpha_{34}) - v_{h34} \sin(\alpha_{40})}{\sin(\delta_{34} - \delta_{40})} \quad (3.3)$$

To find the horizontal wind speed and direction, Eq. 2.6c and Eq.2.6d will be essential. Figure 3-6 illustrates a sketch of the projection of the wind speed on the line-of-sight of a LiDAR laser beam.

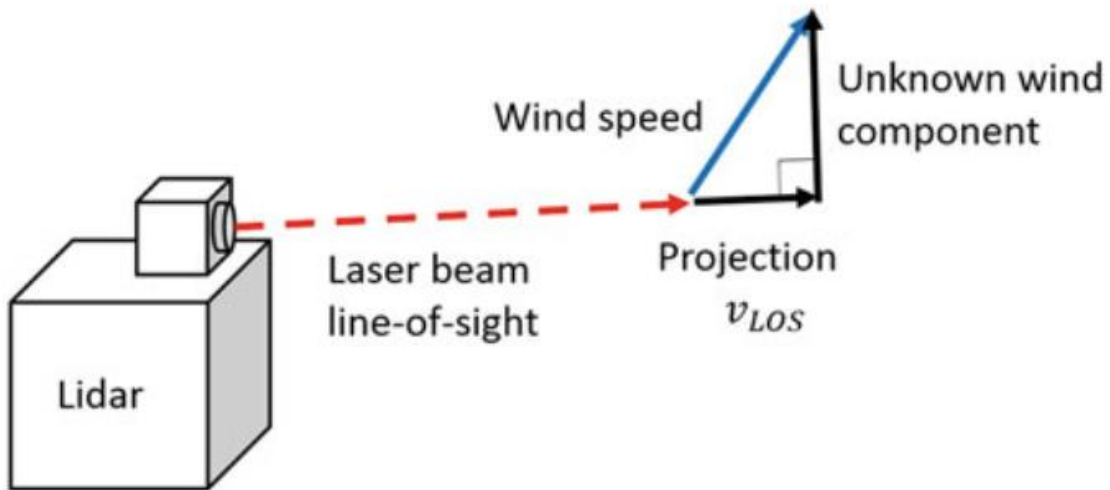


Figure 3-6: Schematic overview of the line-of-sight projection of the wind speed (van Dooren, 2022).

3.2.1.2 Plan position indicator (PPI) scan

Other scan technique capable of a Doppler wind LiDAR is the plan position indicator (PPI) scan. In this case, the scanner head is at a constant elevation angle while the azimuth angle changes continuously with a certain angular speed v_a ($^{\circ} s^{-1}$). Both LiDAR 34 and LiDAR 40 operate within different minutes during the PPI scan mode; for LiDAR 34 the PPI scan mode

runs for 18 minutes within an hour while for LiDAR 40 the PPI scan mode runs for 26 minutes within an hour. For each range gate in the PPI scan, the observed radial velocity v_r is derived from the bulk of particle velocities sampled during a selected integration time τ_i [s]. Therefore, the result is a velocity composite over a certain angular range $\Delta\alpha = v_\alpha \cdot \tau_i$ [°]. A full PPI scan usually corresponds to a complete azimuth angle rotation from $\alpha = 0^\circ$ to $\alpha = 359^\circ$ (Yoshino, 2019), but also PPI scans with smaller azimuth sectors are commonly utilized (Alcayaga, 2020; Krutova et al., 2022). A typical example for PPI scan is the observation of horizontal velocities with a bird’s eye view using a small elevation angle to observe wind turbine wakes on a wind park. Figure 3-7 helps to show schematic view of the PPI scan with a fixed elevation angle and varying azimuth angles

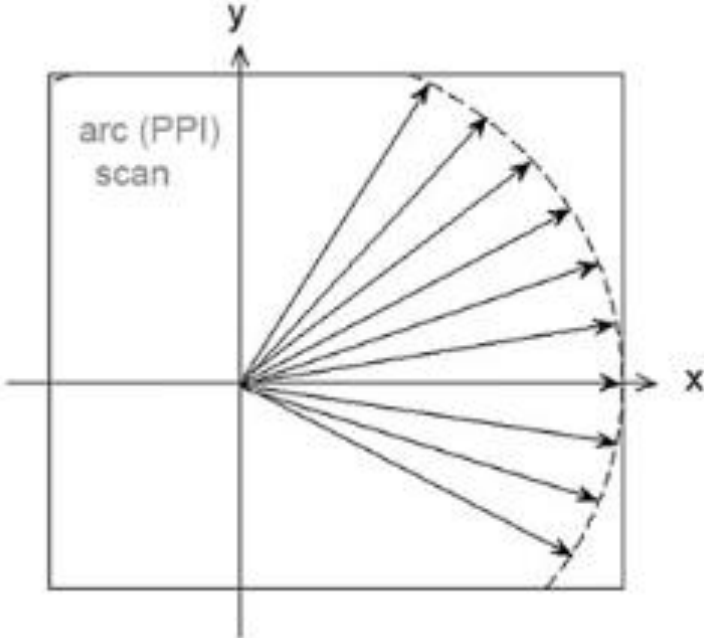


Figure 3-7: PPI scan with varying azimuth angles and a fixed elevation angle (Julia, 2022).

The retrieval of the u, v and w components from a PPI scan can be challenging especially the reconstruction of the 3-D wind vector or a projection of interest. However, from the research done by (Christiane, 2024) it is found that by using the coplanar dual-Lidar retrieval technique, there is a possibility to estimate two of the three wind speed components at several points in space and time.

3.2.1.3 Doppler beam swinging (DBS) scan

The wind scanning LiDAR can also apply a Doppler beam swinging scan pattern, which is a sequence of five single fixed LOS observations. In contrast to the profiling LiDAR, the scanning LiDAR physically rotates its scanner head, changing between different fixed LOS orientations. The scanning LiDAR uses less time during the DBS scan mode compared to the profiling LiDAR, which takes considerably longer to change the beam orientation. Therefore, the order of the sequential beam orientations is optimized for the scanning LiDAR to minimize the time taken. During the LiDAR measurement campaign, LiDAR 40 was the only scanning wind LiDAR configured to run a Doppler beam swinging (DBS) scan. A cycle of the DBS scan was approximately 9 seconds, resulting in 24 DBS scans for each hour that LiDAR 40 was in operation.

The layout in Figure 3-8 illustrates a DBS scan from a scanning LiDAR represented in the x, y, and z directions.

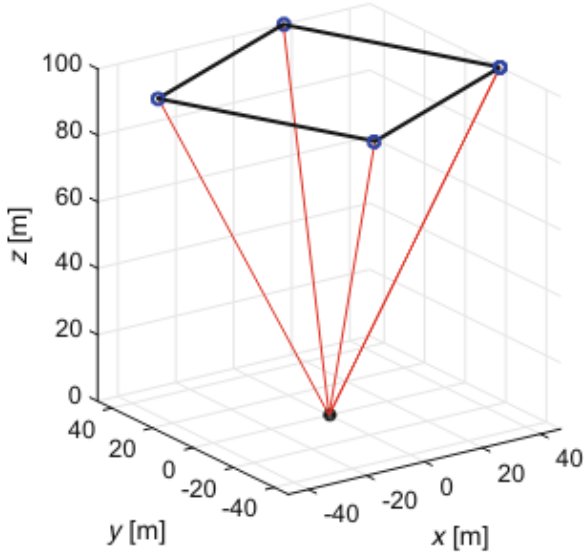


Figure 3-8: Layout of a Doppler beam swing (DBS) LiDAR scan (van Dooren, 2022)

3.3 Data

The availability of rich and dependable data made working on this thesis very interesting. The in-situ measurements shared by Troms Kraft AS were averaged with a 10-minute temporal resolution. The data was collected at the measurement mast present in the Fakken wind park at a height of 80 meters above ground level (a.g.l). The LiDAR scan files were stored by the Doppler wind LiDARs in the form of NetCDF (Network Common Data Form) files, often abbreviated as nc files. The files available were from the 5th of December 2022 to 10th of June 2023. The data files analysed in this thesis was primarily from January 2023 to June 2023. Notably, there were some missing files for some days within the selected months, but January, February, and March had almost complete files for each day. Additionally, a calendar specifically showing the operation days for each LiDAR 34 and LiDAR 40 is in appendix A.

These were the three main set of data provided and used in this thesis.

1. In-situ measurements from the two wind vanes and anemometers at Fakken wind park (Courtesy of Troms Kraft AS)
2. In-situ measurements for each 18 reference wind turbines at Fakken wind park (Courtesy of Troms Kraft AS)
3. Raw LiDAR scan files from two scanning pulsed long-range Doppler wind LiDARS.

3.3.1 LiDAR data processing and cleaning

The analysis and cleaning of LiDAR data are crucial steps in ensuring the accuracy and reliability of wind speed measurement, especially when used for applications such as wind energy assessment. The radial velocity, v_r , data observed by LiDARs can be quite noisy in the case of a low signal-to-noise (SNR). This is usually caused by low airborne particle content. The PPI scan has the potential to feature numerous erroneous patterns, such as range-folded ambiguities resulting from an incorrect range and velocity allocation of the LiDAR beam interacting with distant objects, such as clouds (Bonin & Brewer, 2017). Additionally, obstacles can distort the line-of-sight (LOS) of a LiDAR beam creating erroneous patterns in the observed velocity field.

Although, there are numerous methodologies in filtering noise from LiDAR data, the most common approach is to apply a filter that removes all radial velocity observations below a

certain SNR threshold (Beck & Kühn, 2017). In this thesis, two methods were applied in the process of data filtering. The first step was to refer to the confidence index (%) variable, which is a stored variable of each LiDAR scan (fixed, PPI or DBS). The confidence index (CI) is a data quality indicator, with values of 0 indicating no data or noise and 100 indicating real data.

The second step involved reading the CI variable (radial_wind_speed_ci) into a Pandas dataframe in Python and defining it as a variable (Q1). The third step ensured that after any LiDAR scan file is read for analysis, the radial velocity v_r is passed through Q1 ensuring that every noise point in space and time is replaced with NaN (Not a Number) and each quality data point is replaced with 1. Therefore, a filtered radial velocity vq_r is then created.

The second method applied was the static standard deviation filter, which functions to remove outliers of radial velocity values by choosing a specific standard deviation multiplier. This method ensures that extreme values, which are likely erroneous, are filtered out to maintain the integrity of the dataset.

Figure 3-9 helps to show the effect of filtering noise by confidence index and static standard deviation. This is an example used for a fixed scan of a Doppler pulsed long range LiDAR.

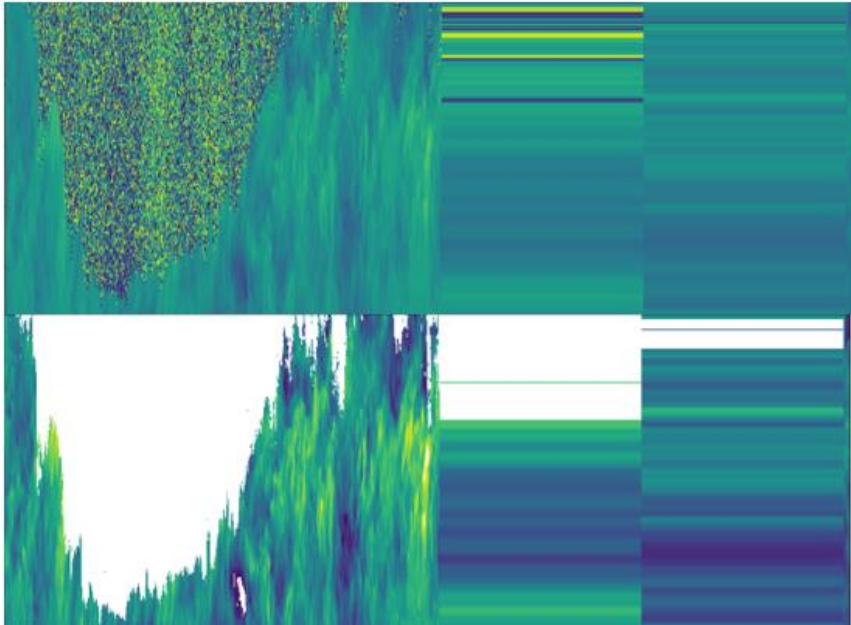


Figure 3-9: Filtering of granular noise from radial velocity v_r observations.

4 Results and Discussion

4.1 Wind rose from fixed LiDAR scans

The wind rose illustrated in the left image of Figure 4-1 shows the potential wind resource at the fixed point in Fakken II for the month of January. The prevailing wind direction is predominantly from the south (S) and southeast (SSE) sectors, with a significant portion of the winds originating from the south-southwest (SSW) direction.

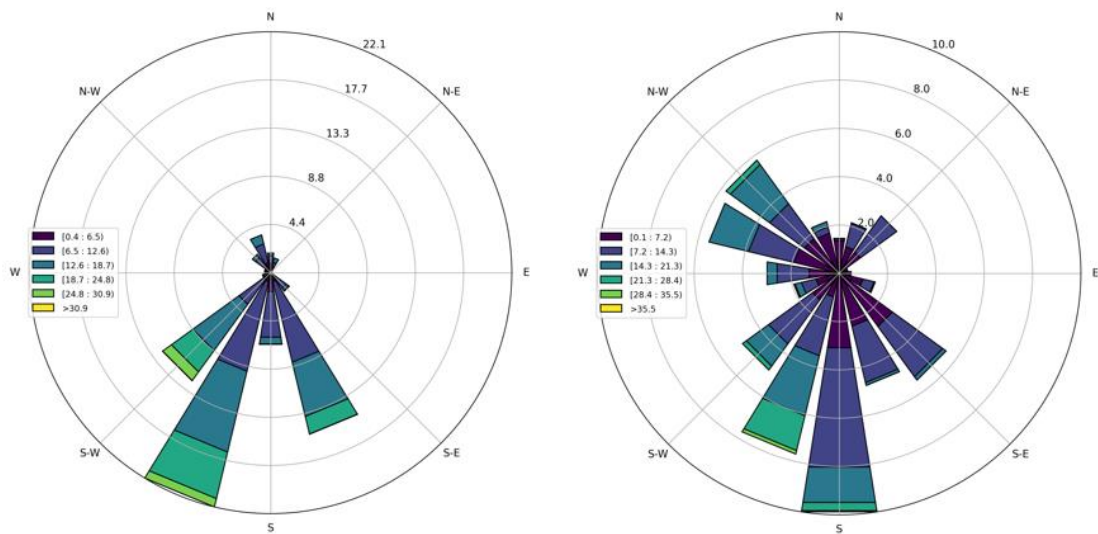


Figure 4-1: Left: Wind rose showing wind resource at the Fakken II fixed point for January 2023. Right: Wind rose showing wind resource at the Fakken II at fixed point for February 2023.

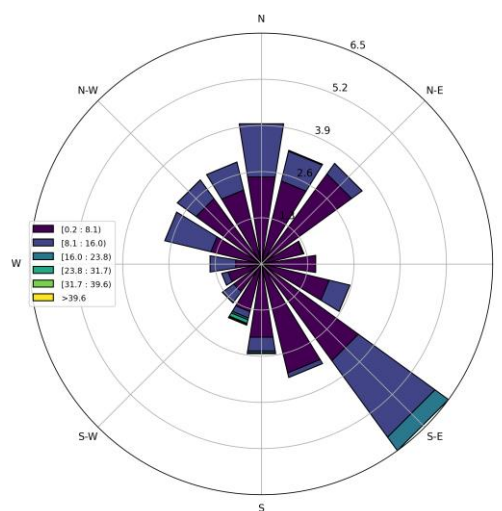


Figure 4-2: Wind rose showing wind resource at Fakken II fixed point for March 2023.

The wind speeds are categorized into bins ranging from 0.4 to over 30.9 m/s, with most wind speeds falling within the 6.5 to 18.7 m/s range, and substantial contributions from the 18.7 to 24.8 m/s range. The wind rose on the right, which represents the wind resource at the fixed point for February, indicates that winds are coming from additional directions such as the northwest and northeast. However, the prevailing winds remain dominant from the south. The wind rose in Figure 4-2 offers a different perspective; it represents the wind resource at the fixed point for March but similarly shows that the prevailing wind is predominantly from the southeast direction, consistent with the other months.

4.2 Wind rose for In-situ measurements from meteorological mast

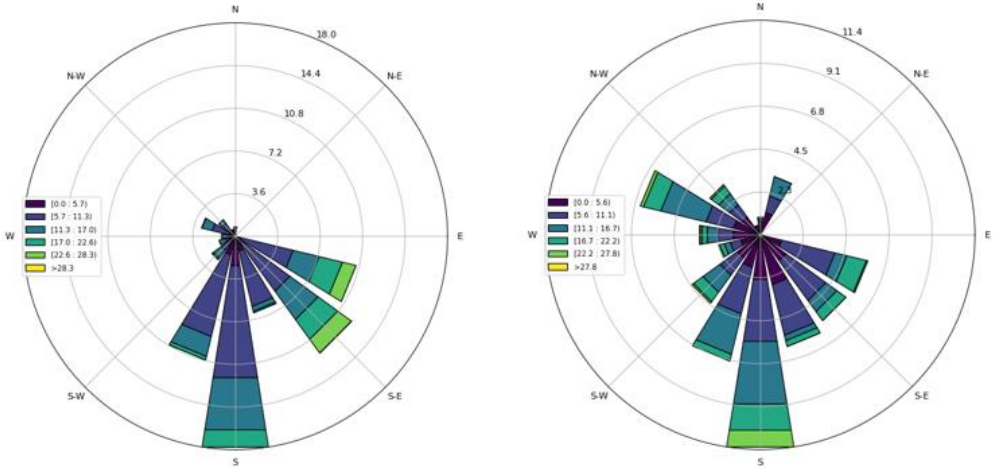


Figure 4-3: Left: Wind rose showing wind resource at Fakken I met-mast for January 2023. Right: Wind rose showing wind resource at Fakken II met-mast for February 2023.

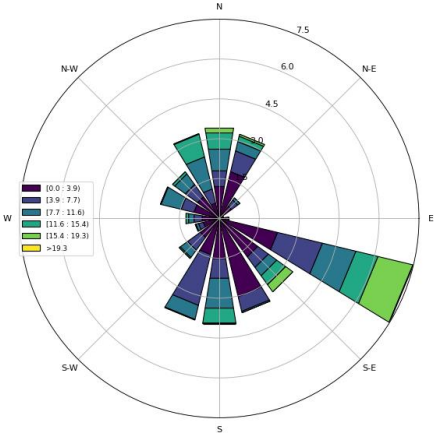


Figure 4-4: Wind rose showing wind resource at Fakken I met-mast for March 2023.

The wind roses in Figures 4-3 and 4-4 illustrate the wind resource at the meteorological mast in Fakken I for January 2023 (left), February (right), and March (center). At first glance, there appears to be consistency in the prevailing wind directions from the south (S), southeast (SSE), and southwest (SSW) when compared to the wind roses obtained from the scanning wind LiDAR. However, the wind speeds seem to be lower, falling within the range of 5 to 22 m/s.

4.3 Wind rose for In-situ measurements from nearest turbine to LiDAR 34

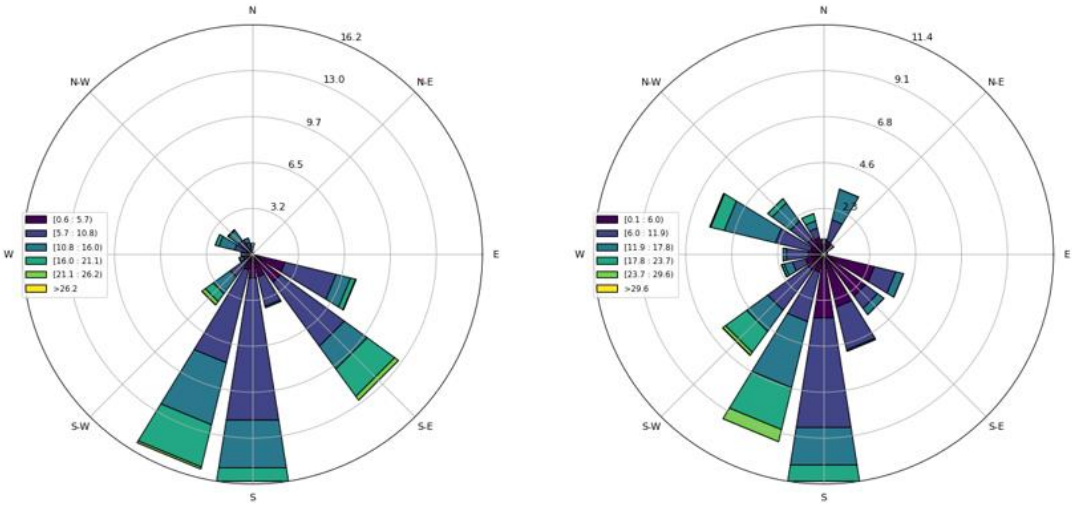


Figure 4-5: Left: Wind rose showing wind resource at WTG10 turbine for January 2023. Right: Wind rose showing wind resource at WTG10 turbine for February 2023.

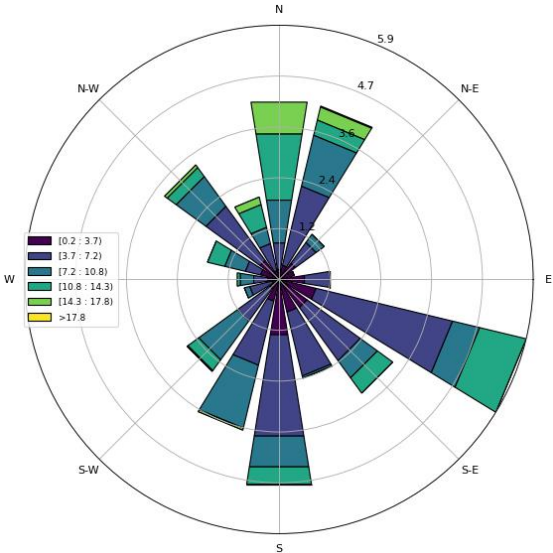


Figure 4-6: Wind rose showing wind resource at WTG10 turbine for March 2023.

The wind roses illustrated in Figures 4-5 and 4-6 are from the nearest turbine (WTG10) to LiDAR 34. Across the three months, the prevailing winds are primarily from the south (S), southeast (SSE), and southwest (SSW) directions. However, the wind rose for turbine WTG10 in March 2023 shows more wind coming from the northwest (NW) to north-northwest (NNW). These winds appear strong but occur with less frequency.

4.4 Wind rose for In-situ measurements from nearest turbine to LiDAR 40

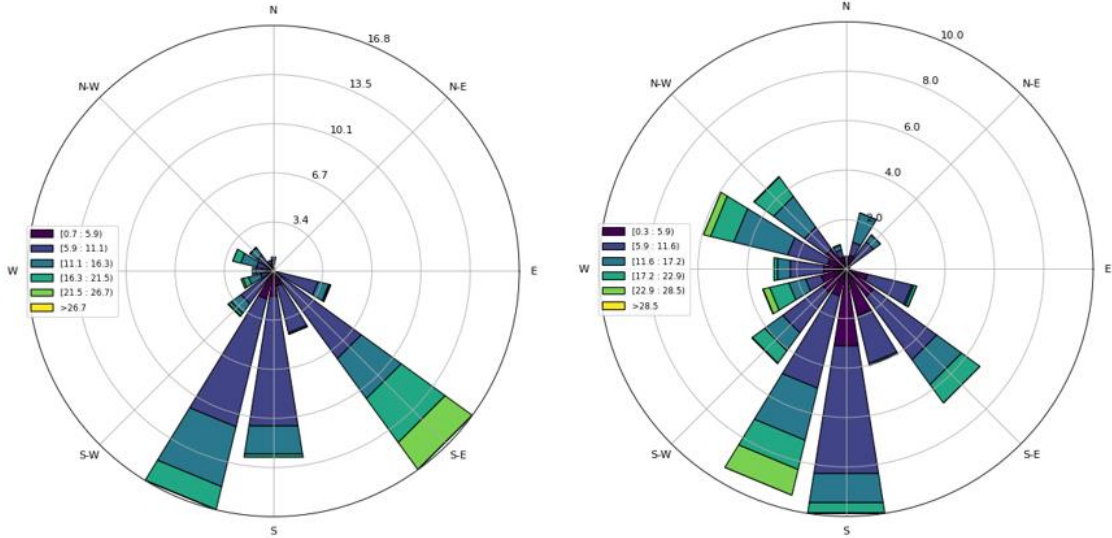


Figure 4-7: Left: Wind rose showing wind resource at WTG15 turbine for January 2023. Right: Wind rose showing wind resource at WTG15 turbine for February 2023.

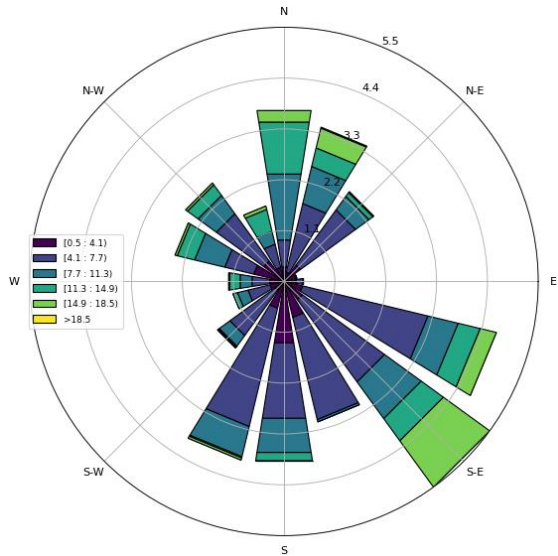


Figure 4-8: Wind rose showing wind resource at WTG15 turbine for March 2023.

The wind roses illustrated in Figures 4-7 and 4-8 provide valuable insights into the wind resource at the WTG15 turbine, which is closest to LiDAR 40. In January 2023, the highest frequency wind speed range is between 5.9 and 11.1 m/s. In February, more wind is observed coming not only from the dominant south (S), southwest (SW), and southeast (SSE) directions but also from the west (W) and northwest (NW) directions. The wind rose for March 2023 shows an increase in higher wind speeds, although these occur with lower frequency. It is noteworthy that the wind roses in Figures 4-6 and 4-8 share a similar outlook, with the primary difference being the higher wind speed range (>18.5 m/s) observed in Figure 4-8.

4.5 Correlation Test

4.5.1 Wind speed time series correlation for LiDAR wind data and met-mast (January 2023).

To assess the accuracy of the extracted LiDAR wind data, it is required and advisable to find the degree of agreement between the reference wind speed data from the met-mast and wind speed data obtained from the LiDARs. A time series correlation plot can help give more understanding to the degree of agreement. The period of comparison is January 2023. This comparison ought to give a valuable insight into the reliability of the LiDAR wind data.

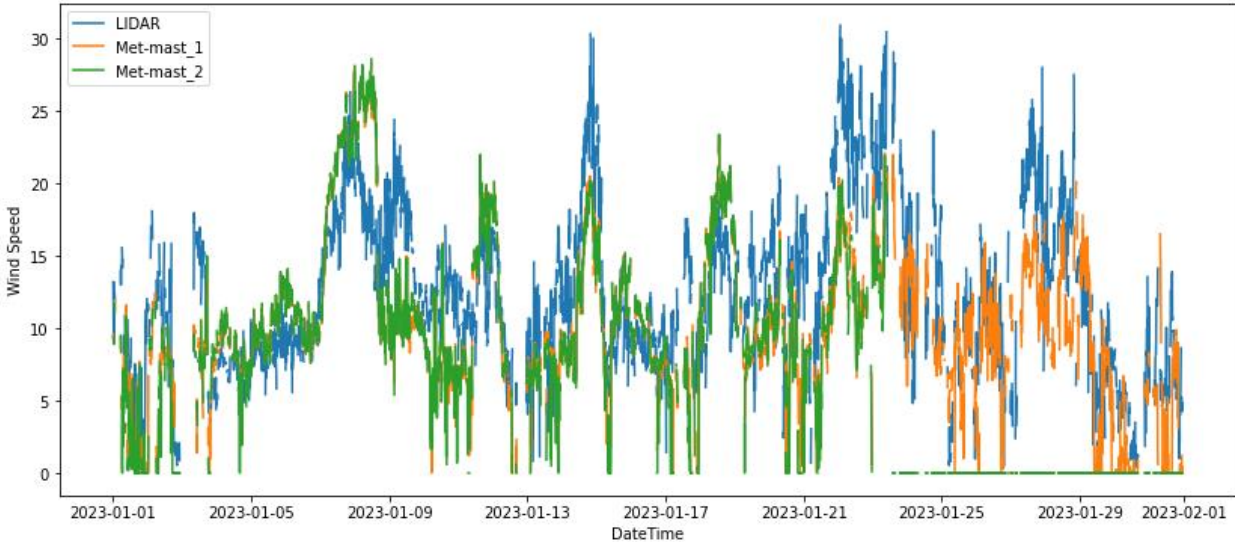


Figure 4-9: Time series correlation between wind speed from LiDAR and wind speed from met-mast.

Figure 4-9 visually represents the correlation between the wind speeds from the LiDAR data and those obtained from the anemometers on the met-mast. The blue line represents the LiDAR data, the orange line represents met-mast 1, and the green line represents met-mast 2. At first glance, the LiDAR wind speeds appear to have minimal deviation compared to the met-mast data. However, upon closer examination, significant deviations become apparent in the time series plot on January 13th, between January 21st and 25th, and on January 29th. The LiDAR wind speeds tend to overestimate those recorded by the met-masts.

Additionally, Figure 4-10 presents a correlation matrix for the same wind speed data from the LiDAR and met-masts. In this matrix, a value of 1.0 indicates a strong correlation, while 0.5 indicates a weak correlation between the data samples. However, upon closer examination of the correlation matrix, it is evident that the LiDAR data has a stronger correlation (0.61) with met-mast 1 data compared to a weaker correlation (0.43) with met-mast 2 data.

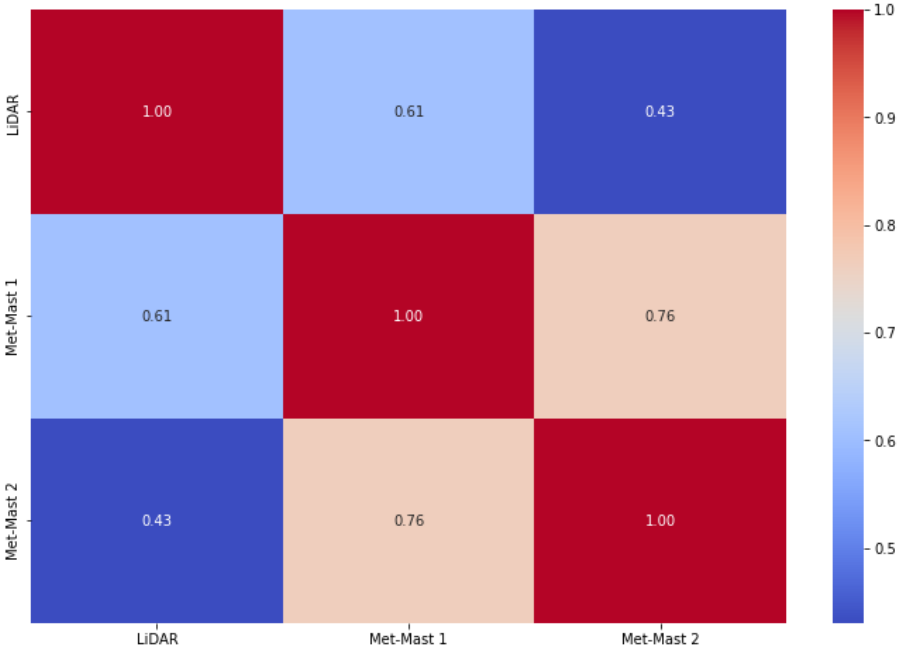


Figure 4-10: Correlation matrix between LiDAR data sample and Met-Mast data sample.

To understand the overestimation effect by the LiDAR data, refer to Figure 4-11, which shows a time series plot for a week (16th – 22nd) in January. The week-based time series plot provides a clearer insight into the overestimation effect. It is now evident that there is a discrepancy between the LiDAR data and the met-mast data.

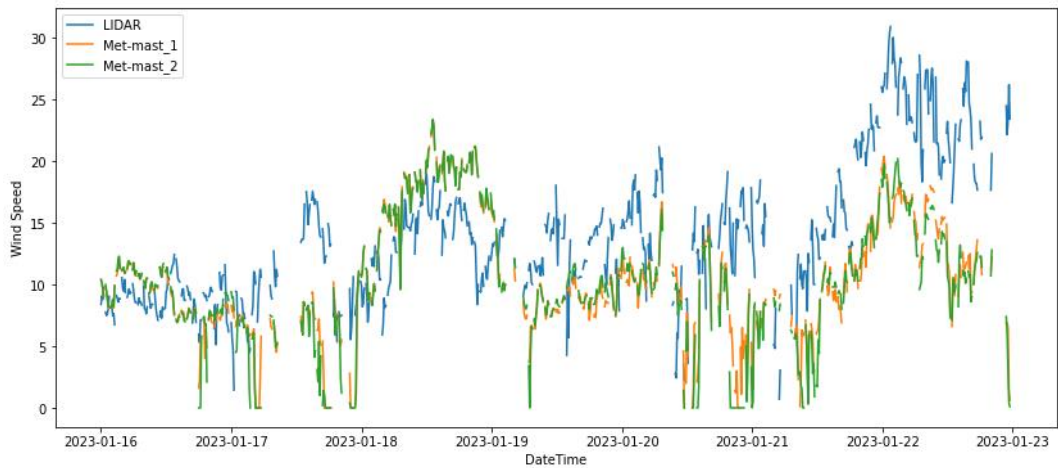


Figure 4-11: Time series correlation plot for a week in January 2023

4.5.2 Wind speed time series correlation for LiDAR wind data and met-mast (February 2023).

The time series plot in Figure 4-12 compares the wind speed data from the LiDAR against the data from the met-mast for the month of February. This comparison is one-to-one between the LiDAR and met-mast data. As expected, there are overlaps in the blue curve, similar to Figure 4-9, which likely result from the overestimation of wind speed by the LiDAR. To further analyse this, a detailed examination of the time series representation for a week within February will be conducted to determine if the discrepancy between the LiDAR and met-mast data is consistent.

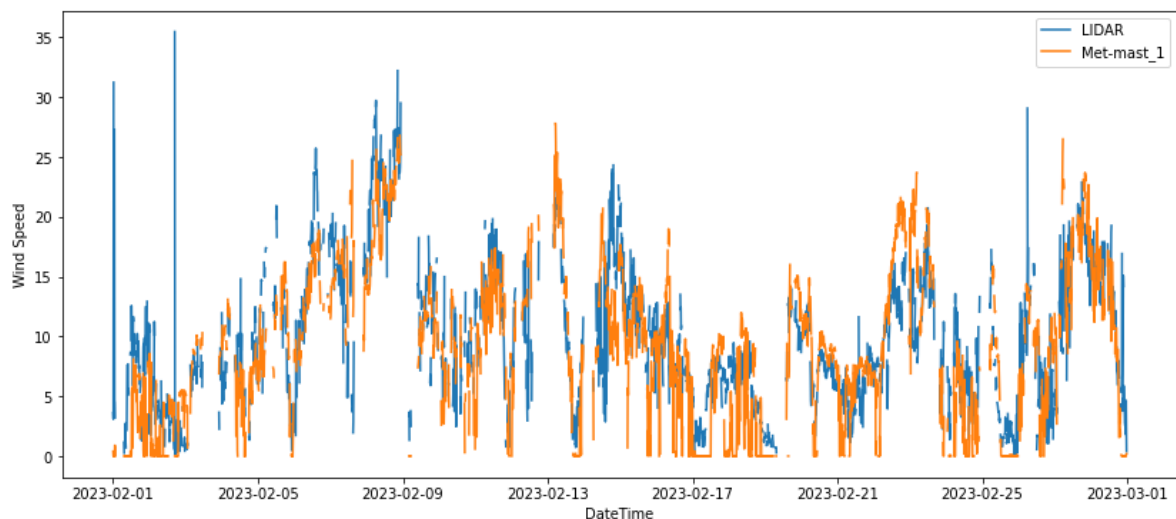


Figure 4-12: Time series correlation between wind speed from LiDAR and wind speed from met-mast.

Figure 4-13 provides a closer look at this comparison for a specific week in February. From this plot, it is evident that the LiDAR wind data does not align well with the met-mast wind data, with the LiDAR data curve being overlapped by the met-mast data. At this point, it is premature to conclusively state that the LiDAR wind data consistently overestimates the met-mast wind data. Accurate data estimates are crucial for planning new wind parks.

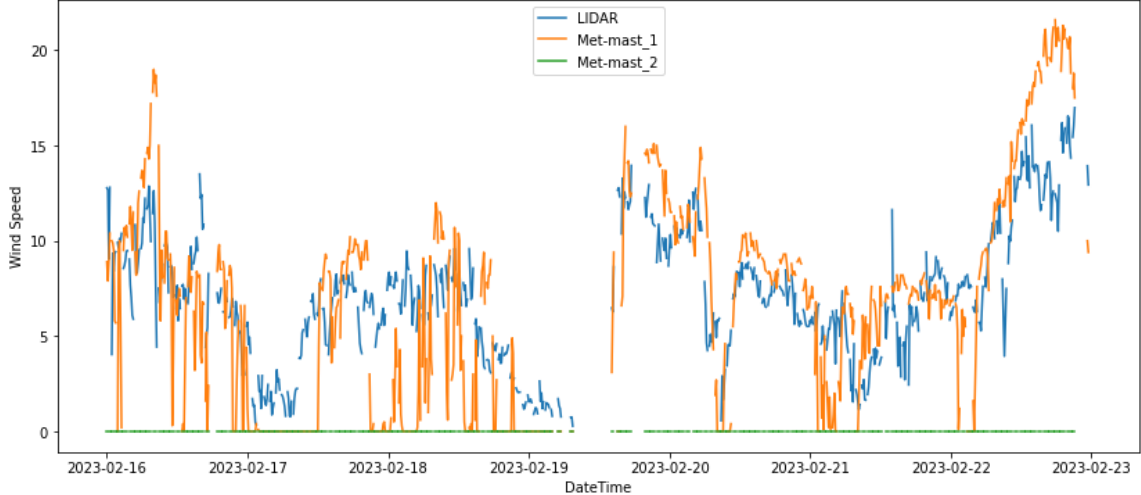


Figure 4-13: Time series correlation plot for a week in February 2023.

Studies have investigated the accuracy of wind data obtained by LiDARs. (Bingöl et al., 2009) found that LiDAR errors can reach up to 10%, especially in complex terrain where wind flow is inhomogeneous. (Harris et al., 2010) concluded that CFD models can better estimate LiDAR errors caused by atmospheric conditions affecting the LiDAR beam, particularly at higher altitudes. These cases underscore the importance of using meteorological masts as benchmarks for validating and trusting LiDAR wind data.

4.6 Histogram of wind speed and Weibull distribution plot for LiDAR wind speed data and met-mast speed data

The histogram and Weibull distribution plots in Figures 4-14 and 4-15 are presented to compare the long-term distribution of wind speed at a fixed point in Fakken II with met-mast wind data. Both data samples are from January 2023.

Figure 4-14 displays a histogram plot representing observed wind speed frequencies on the right, while the red curve on the left indicates the fitted Weibull PDF. Key parameters (shape parameter in red, scale parameter in blue) are annotated on the Weibull distribution plot.

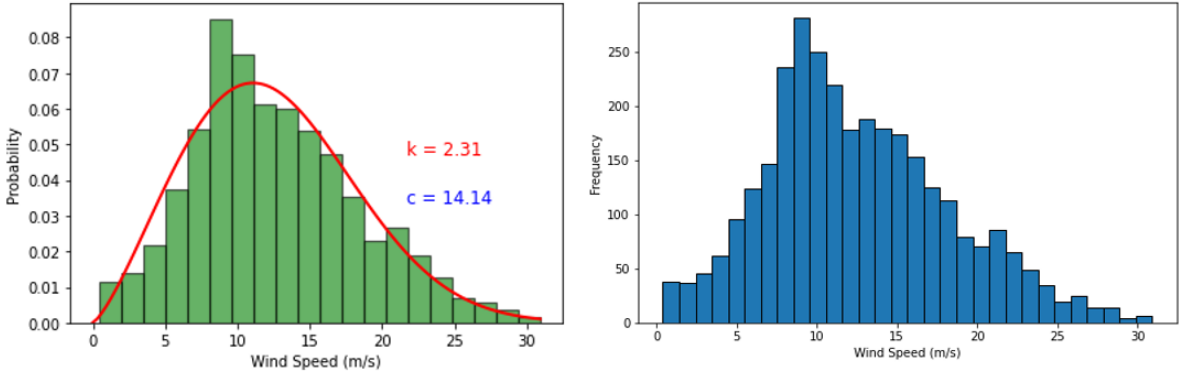


Figure 4-14: Left: Weibull distribution for LiDAR wind speed data. Right: Histogram plot of LiDAR wind speed data

For the LiDAR wind speed data, the Weibull distribution has a shape parameter of 2.31 and a scale parameter of 14.14. A shape parameter of $1 < k < 3$ indicates a distribution that is moderately right skewed. This suggests that while there are occasionally high wind speeds, they are less frequent compared to lower and moderate wind speeds. The tail extending to the right further implies that high wind speeds are present but infrequent.

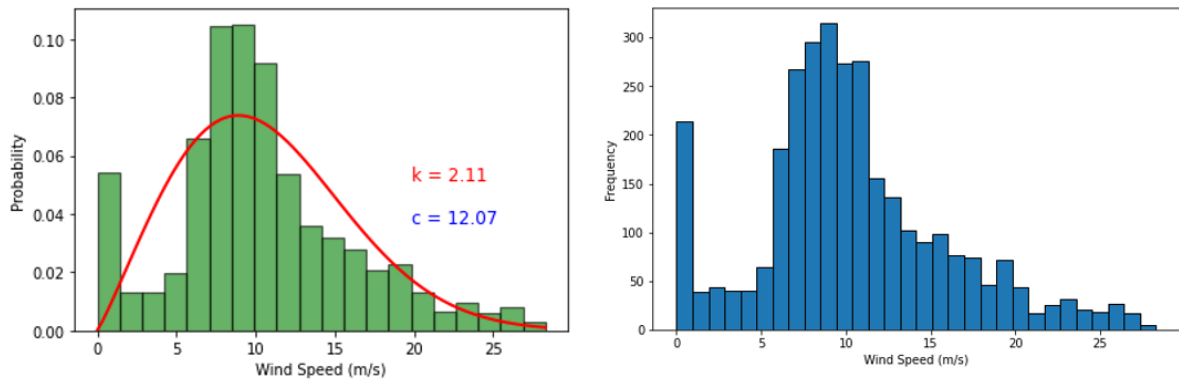


Figure 4-15: Left: Weibull distribution for met-mast wind speed data. Right: Histogram plot of met-mast wind speed data.

In Figure 4-15, the Weibull distribution plot having a shape parameter k slightly greater than 2 indicates a moderately right skewed distribution. Most of the data is concentrated around lower to moderate values, with a tail extending towards higher wind speeds. The scale parameter c of 12.07 stretches the distribution along on the x-axis, meaning that wind speed values are centred around this value, with the most frequent wind speed (mode) being slightly lower.

Comparing the insights from the histogram and Weibull distribution plots in Figure 4-14 and 4-15 both wind speed distributions are right skewed. The distribution with a scale parameter of 14.14 suggests higher wind speeds on average compared to the distribution with a scale parameter of 12.07, indicating that wind speeds are generally higher in the LiDAR data. The met-mast wind data shows greater variability, with a wider range of wind speed values, suggesting it is more spread out.

Both the LiDAR and met-mast wind speed distributions indicate good potential for energy generation. However, the higher and more consistent wind speeds from the fixed point at Fakkem II suggest more reliable energy production at that location.

4.7 Estimation of wind energy production from LiDAR wind data

After obtaining and analyzing wind speed data from both LiDARs scanning over the fixed point designated to serve as the met-mast for Fakken II during the period from January to March 2023, the next step is to estimate energy production, a crucial factor in wind turbine siting. The wind speed data were measured in meters per second (m/s). The observed energy production from each turbine at Fakken I during the specified period (January to March 2023) is illustrated in Figure 4-16. Turbine F, situated at coordinates 70.1055° latitude and 20.01247° longitude, emerges as the closest turbine to the fixed point in Fakken II. Given the proximity of Turbine F to the fixed point, it can be inferred that there will be little to no difference in the wind resource available at both locations. This inference is supported by previous studies on wind patterns in similar terrain. Consequently, we will continue to utilize the wind data acquired at the fixed point for estimating wind energy production at Turbine F. However, it is important to acknowledge potential limitations, such as variations in wind speed and direction across different heights and terrain features, which may affect the accuracy of the estimates.

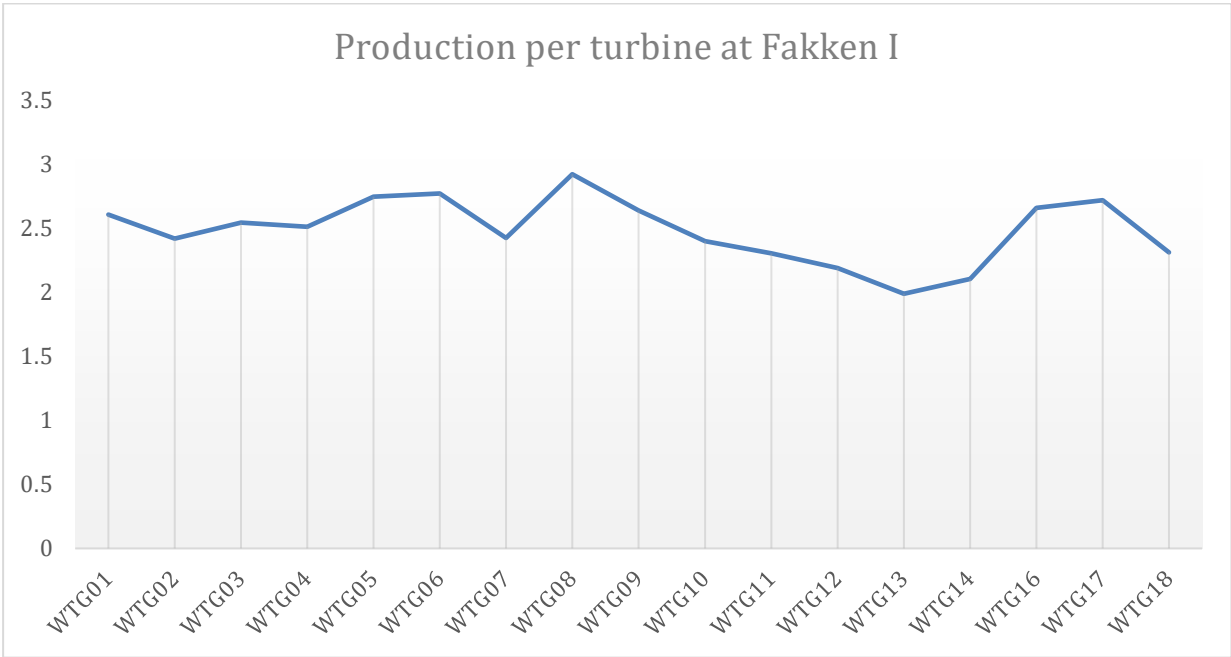


Figure 4-16: Energy production within January to March 2023 for each turbine at Fakken I.

Once the wind power production at Turbine F in Fakken II is determined, it will be compared with the observed power production of some turbines in Fakken I that closely aligns with the LiDAR wind data in terms of wind speed and direction. This comparison is crucial to ensure accuracy across the board, requiring a strong correlation between the data samples from the selected turbines and the LiDAR.

In estimating the wind power production at Turbine F, the two elements required are the power curve of the Vestas V90-3.0MW and the 10-minute averaged wind speed data from the fixed point in Fakken II. The power curve data was obtained from manufacturer specifications. An interpolation of the power output values for each wind speed from the power curve was applied on the wind speed data from the fixed point using linear interpolation, and the result was a 10-minute averaged power production from January to March 2023. Figure 4-17 shows the estimated energy production at Turbine F in Fakken II.

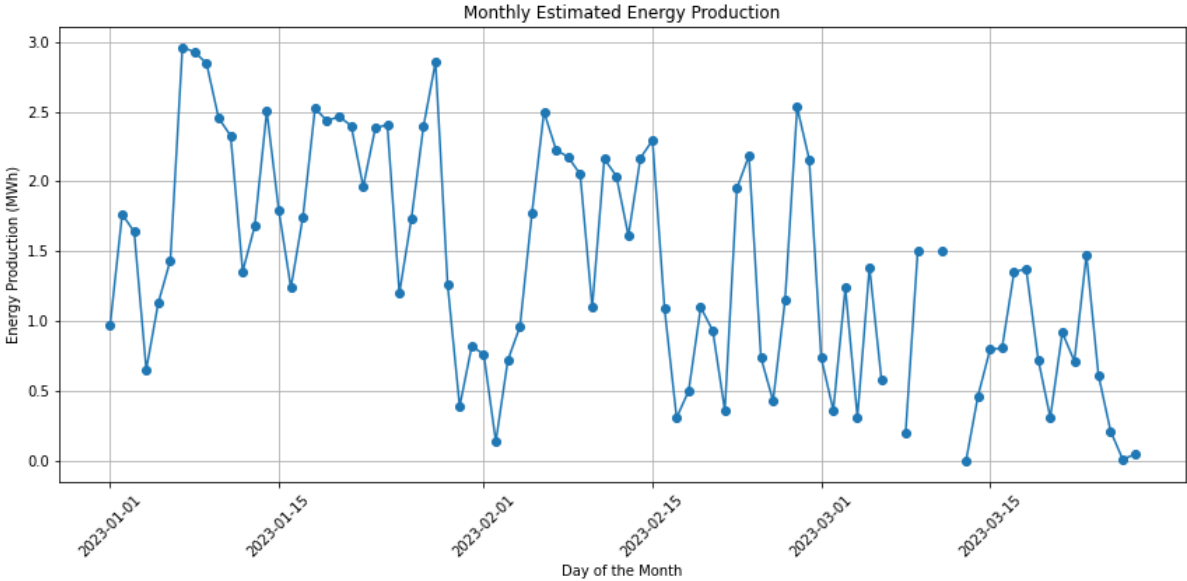


Figure 4-17: Estimated energy production within January to March 2023 for Turbine F at Fakken II.

The above Figure 4-17 shows the variance of the estimated energy that will likely be produced at the location of Turbine F in the expanded region of the Fakken wind park. It can be deduced from the plot that the most consistent and high-value energy was produced in January, ranging from 1.6 MWh to 3 MWh. The energy produced in the later months of February and March exhibited some consistency but with occasional periods of energy drop. Wind energy production typically exhibits a linear correlation with wind speed. Therefore, under normal

operating conditions, a wind turbine should produce energy closest to its rated power when the available wind speed is consistent and high.

The correlation analysis identified turbines WTG06, WTG09, WTG10, and WTG14 in Fakken I as consistently demonstrating good agreement with the LiDAR (Turbine F) wind data. As depicted in Figure 4-16, the estimated wind energy production from turbine WTG08 peaks at approximately 2.92 GWh, while turbine WTG13 is the lowest-producing turbine at approximately 1.99 GWh.

The subsequent step involves performing a statistical evaluation between the estimated wind energy production from the four turbines (WTG06, WTG09, WTG10, and WTG14) in Fakken I and turbine F in Fakken II. An estimation error between both turbine productions will be assessed by analysing the deviation between the model's estimated value (Turbine F) and the observed values (WTG06, WTG09, WTG10, WTG14). The statistical metrics necessary for this evaluation are explained in Chapter 2.6 of this thesis.

The table below presents the estimation error in energy production between Turbine F in Fakken II and turbines WTG06, WTG09, WTG10, and WTG14 in Fakken I.

Table 4-1: Statistical evaluation of the estimated energy production from the model and observed data.

	RMSE evaluation	MAE evaluation	MAPE evaluation	Bias evaluation
WTG06 vs Turbine F	0.929	0.630	782.71%	0.089
WTG09 vs Turbine F	0.933	0.635	724.04%	0.229
WTG10 vs Turbine F	1.039	0.708	3586.44%	0.320
WTG14 vs Turbine F	1.194	0.820	4197.61%	0.516

The values in the above table show the results from using statistical metrics to evaluate the performance of predictive models, specifically the estimated energy production for Turbine F. Four metrics were employed: Root Mean Square Error (RMSE), Bias, Mean Absolute Error (MAE), and Mean Absolute Percentage Error (MAPE).

From the statistical evaluation results, the model's estimated values for Turbine F are closest to the observed values from turbine WTG06 when compared to the other three turbines. These statistical metrics are negatively oriented scores, meaning that lower values indicate better accuracy between the estimated value of the model (Turbine F) and the observed values from the outlined turbines. The results consistently show that the "WTG06 vs Turbine F" comparison achieves the lowest values across all statistical metrics except for the MAPE metric. MAPE, expressed as a percentage, measures the average of the absolute percentage errors between predicted and actual values. A lower MAPE indicates better accuracy.

The high MAPE results in Table 4-1 suggest the presence of small or zero values in the observed energy production estimates from the outlined turbines in Fakken I. Further analysis of the dataset revealed a significant presence of zero and negative values, particularly concerning the negative values, which are unexpected for energy production data.

It's likely that these negative values resulted from data processing errors, invalid data recorded during turbine downtime, or faulty calibration of measurement instruments. To address this issue, appropriate data handling techniques were implemented: (i) checking and removing NaN values, (ii) filtering out negative values before running the statistical evaluation, and (iii) setting minimum and maximum thresholds (min_threshold = 0.01 MWh & max_threshold = 50 MWh) for observed energy production estimates to avoid evaluating statistical metrics with insignificant values that could skew the results.

The aftermath of applying these data handling techniques is reflected in the results found below in Table 4-2.

Table 4-2: Results of statistical evaluation after applying data handling techniques.

	RMSE evaluation	MAE evaluation	MAPE evaluation	Bias evaluation
WTG06 vs Turbine F	0.864	0.604	109.40%	0.025
WTG09 vs Turbine F	0.896	0.634	133.02%	0.192
WTG10 vs Turbine F	0.891	0.636	158.34%	0.199
WTG14 vs Turbine F	0.914	0.649	138.48%	0.270

The new results demonstrate a significant reduction in the Mean Absolute Percentage Error (MAPE) for all four statistical evaluations, indicating a marked improvement in accuracy. Additionally, there is a slight decrease in the Root Mean Square Error (RMSE), Mean Absolute Error (MAE), and Bias results for all instances of statistical evaluation. The MAPE evaluation results still looking high despite using the data handling techniques show that a large percentage of the dataset from the observed energy production estimates have a high degree of variability. This variability could be due to intermittent wind conditions, operational issues with the turbines, or residual data quality issues that were not fully mitigated by the applied data handling techniques.

The persistence of high MAPE values suggests that further refinement of data processing methods might be necessary. This could involve more advanced techniques for handling outliers, improving the accuracy of data during periods of turbine downtime, or employing more sophisticated statistical models that can better account for variability and uncertainty in the observed energy production data. Continuous monitoring and validation of the data collection process are essential to ensure the reliability and accuracy of the energy production estimates, thereby improving the predictive performance of the model.

The evaluation results from "WTG06 vs Turbine F" remain the lowest, suggesting that the wind energy estimated to be produced at Turbine F closely aligns with the energy production at WTG06 in Fakken I. This consistency implies that the estimated energy production at WTG06 falls within the same range as that of Turbine F located in Fakken II. The instances of "WTG09 vs Turbine F" and "WTG10 vs Turbine F" yield similarly low evaluation results. This is likely due to the proximity of turbines WTG09 and WTG10 to Turbine F, where their close distance minimizes the impact of wind variability on energy production estimation. Therefore, the estimated energy production at Turbine F is expected to be comparable to that of WTG09 and WTG10, given their proximity and similar wind conditions.

4.7.1 Using WAsP for turbine siting at Fakken II

WAsP is an excellent tool for wind resource assessment, optimized for microscale flow analysis, and it incorporates a resource grid feature beneficial for turbine siting in wind parks. While the WAsP software was not directly employed as a methodology in this thesis, it served as a significant reference point. Much of the relevant literature and methodologies were drawn from a previous thesis by (Bjugg, 2023), which provided motivation for the development of this thesis.

As illustrated in Figure 4-17, the WAsP tool helps to define resource grids positioned over Fakken I and Fakken II. These grids correspond to the turbine hub height within each zone. Resource grids are crucial for providing information about average wind speeds. The zones highlighted in red indicate areas with the highest mean wind speeds, suggesting that turbines placed within these areas have high potential for significant energy production.

The WAsP tool features high computational power, allowing for rapid estimation of energy production once the positions of each turbine are inputted into the tool. In contrast, other wind resource assessment tools would take longer to achieve the same results.

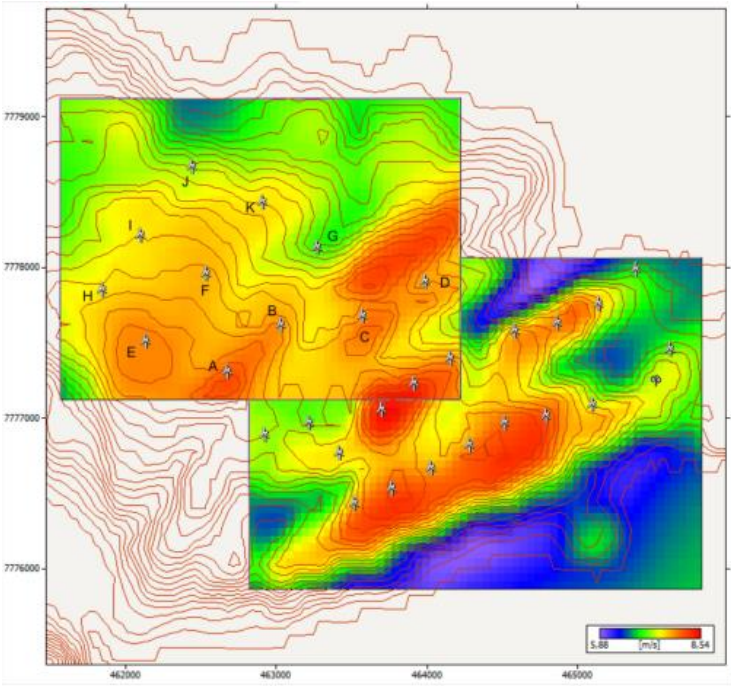


Figure 4-18: Resource grid from WAsP over Fakken I and Fakken II (Bjugg, 2023).

Using the WAsP tool offers the advantage of readjusting turbine positions and recalculating energy production to check for improvements. As seen in Figure 4-18, the spacing between turbines can significantly impact wake losses on wind flow, potentially affecting overall annual energy production (AEP). The WAsP tool includes a feature for evaluating wake losses within selected areas, although it tends to underestimate these losses, a factor that should be considered when interpreting the results.

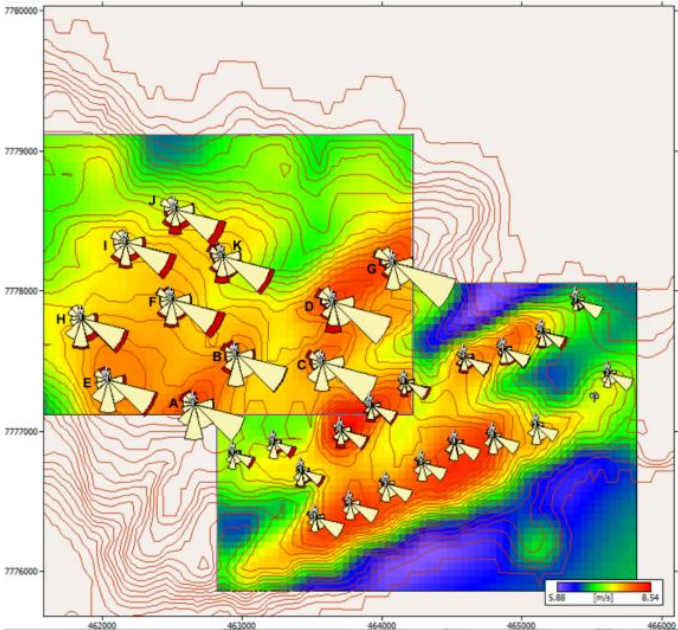


Figure 4-19: Resource grid from WAsP showing wind roses indicating gross AEP and potential wake losses (Bjugg, 2023).

Figure 4-18 shows that wake losses are present but not significantly pronounced. It can be inferred that Fakken II could be affected by Fakken I, as prevailing winds from the southeast direction, after flowing past Fakken I, will lose a significant amount of energy before reaching Fakken II. Contributing factors to these effects include different turbine heights at Fakken I and Fakken II, the complex terrain surrounding both wind parks, and the WAsP tool's tendency to underestimate wake losses.

A better understanding of Figure 4-18 indicates that the front row turbines at Fakken II will not experience wake losses from Fakken I. However, there is a chance that the mid-row turbines in Fakken II will cause a wake effect on the front row turbines. Since the WAsP tool provides insights into the presence of wake losses in Fakken I, implementing Fakken II could introduce additional wake effects.

Wind direction can change throughout the year, as shown by the wind roses in Chapter 4, which illustrate wind direction changes from January to March. Even though winds from the north, as depicted in Figure 4-18, will initially pass through Fakken II and result in reduced wind speeds upon reaching Fakken I, this reduction is expected to be negligible in terms of energy production at Fakken I.

Reassessing turbine positions at Fakken II can maximize energy production. The proposed turbine coordinates listed in Appendix B is the result of the minor adjustments made to account for wake losses. Although these adjustments are not massive, they contribute to an increase in the gross AEP from Fakken II. Figure 4-19, originally from (Bjugg, 2023), shows that repositioning turbines D and G, along with other minor adjustments, added an effect of 6.8 GWh to the sampled 2017 data from Fakken II.

Simulation	Total yearly production (GWh)
WAsP Fakken 2 (2017)	173,9
WAsP Fakken 2 (2017)*	180,7

Figure 4-20: Effect of repositioning turbines at Fakken II adding to the yearly energy production from a sampled 2017 data (Bjugg, 2023).

5 Conclusion

5.1 Summary and key findings

The aim of this thesis was to study the wind conditions for the planned expansion of the Fakken wind park, known as "Fakken II." This investigation utilized two pulsed long-range Doppler LiDARs to scan the designated area and collect wind-related data. The raw LiDAR scan files contained the radial velocity parameter, which was essential for assessing and transforming the data into useful illustrations, such as wind roses and histograms. These visualizations were crucial for analysing the potential energy production from the expanded wind park.

One of the initial observations during the LiDAR data processing was the substantial absence of files for several days within the LiDAR measurement campaign. This issue necessitated extensive file sorting to ensure the completeness of the dataset, ultimately focusing on the period from January 2023 to March 2023. The missing files were attributed to downtime due to maintenance activities on the LiDAR units at certain points during the measurement period. An intensive data cleaning technique was applied to the selected files to remove noise caused by airborne particles.

Presented below are key findings from analysis of the wind data obtained from the fixed scans of the Doppler LiDARs:

- **Wind Speed and Direction Analysis:**

- The analysis of the LiDAR data revealed that the predominant wind directions were from the northwest and southeast, consistent with the general wind patterns observed in the region.
- The wind speed data indicated that the highest wind speeds were recorded in January 2023, with a gradual decrease observed in February and March 2023, aligning with typical seasonal variations.

- **Energy Production Estimation:**

- The estimated energy production for Turbine F in Fakken II was calculated using the power curve of the Vestas V90-3.0MW turbine and the 10-minute averaged wind speed data from the fixed point in Fakken II. The results indicated that January had the most consistent and highest energy production, ranging from 1.6 MWh to 3 MWh.
- The comparison of estimated energy production between Turbine F and turbines in Fakken I (WTG06, WTG09, WTG10, and WTG14) showed that Turbine F's estimates closely align with WTG06, suggesting similar wind resource availability.

- **Accuracy of LiDAR Wind Data:**

- The time series correlation plot and correlation matrix for January 2023 revealed that the LiDAR wind speeds tend to overestimate those recorded by the met-masts, with significant deviations on specific dates.
- The correlation matrix indicated a stronger correlation between the LiDAR data and met-mast 1 (0.61) compared to met-mast 2 (0.43).
- Further detailed time series analysis for specific weeks in January and February confirmed the overestimation effect, highlighting discrepancies between the LiDAR and met-mast data.

- **Statistical Evaluation:**

- Statistical evaluation metrics (RMSE, MAE, Bias, and MAPE) highlighted that "WTG06 vs Turbine F" consistently had the lowest error values across all metrics, indicating a strong correlation between the wind data at these locations.
- The application of data handling techniques, including the removal of NaN values, filtering out negative values, and setting thresholds, significantly improved the accuracy of the statistical evaluations. However, high MAPE values persisted, suggesting the presence of high variability in the dataset.

- **Data Quality and Limitations:**

- The analysis identified several limitations, including the presence of zero and negative values in the observed energy production data, likely due to data processing errors, downtime during turbine operations, or faulty calibration of measurement instruments.
- Further refinement of data processing methods is necessary to address these issues and improve the reliability and accuracy of the energy production estimates.

- **Weibull Distribution Analysis:**

- The Weibull distribution analysis for both LiDAR and met-mast wind speed data indicated moderately right-skewed distributions. The LiDAR data showed a higher average wind speed (shape parameter 2.31, scale parameter 14.14) compared to the met-mast data (shape parameter slightly above 2, scale parameter 12.07).
- The higher and more consistent wind speeds from the fixed point at Fakken II suggest more reliable energy production at that location.

WASP is a valuable tool for wind resource assessment, offering efficient microscale flow analysis and resource grid features crucial for turbine siting. While not directly used in this thesis, it served as an important reference. WASP's ability to quickly estimate energy production and evaluate wake losses highlights its utility. Analysis showed that repositioning turbines based on WASP's insights can significantly increase energy production, as demonstrated by the 6.8 GWh improvement in Fakken II with minor adjustments.

5.2 Future work

The findings of this thesis have shed light on several key aspects of wind resource assessment in the context of the planned expansion of the Fakken wind park. However, there are still avenues for further exploration and refinement that could enhance the accuracy and reliability of wind data analysis in the future.

Firstly, it is important to acknowledge that while this study has provided valuable insights into the potential of using LiDAR as a wind resource assessment tool, more comprehensive data collection is necessary to fully justify its efficacy as a substitute for meteorological masts. The focus period of three months, while informative, may not capture the full range of wind patterns and variations that occur over longer timeframes. Therefore, additional LiDAR data collection over an extended period would be beneficial to assess its long-term performance and reliability accurately.

Despite the limited timeframe of the study, the results have demonstrated promising correlations between LiDAR data and data obtained from meteorological masts. This suggests that LiDAR has potential as a wind resource assessment tool, especially when supplemented with additional data and analysis techniques. Utilizing LiDAR data in conjunction with the WAsP tool could provide more comprehensive insights into wind resource availability and turbine siting. However, to fully leverage the capabilities of WAsP and ensure accurate assessments, a longer time series of wind data from LiDAR scans would be advantageous.

In conclusion, while this study has provided valuable insights into wind resource assessment using LiDAR technology, there are still opportunities for further research and refinement. By continuing to explore and validate the capabilities of LiDAR in wind resource assessment, researchers can contribute to the advancement of wind energy technologies and facilitate more informed decision-making in wind farm development projects.

Bibliography

- Abdi, D. S., & Bitsuamlak, G. T. (2014). Wind flow simulations on idealized and real complex terrain using various turbulence models. *Advances in Engineering Software*, 75, 30-41. <https://doi.org/10.1016/j.advengsoft.2014.05.002>
- Ahrens, C. D. R., Henson. (2019). *Meteorology Today: An Introduction to Weather, Climate, and the Environment* (13E ed.). Cengage.
- Ainslie, J. F. (1988). Calculating the flowfield in the wake of wind turbines. *Journal of Wind Engineering and Industrial Aerodynamics*, 27(1-3), 213-224. [https://doi.org/10.1016/0167-6105\(88\)90037-2](https://doi.org/10.1016/0167-6105(88)90037-2)
- Alcayaga, L. (2020). Filtering of pulsed lidar data using spatial information and a clustering algorithm. *Atmospheric Measurement Techniques*, 13(11), 6237-6254. <https://doi.org/10.5194/amt-13-6237-2020>
- Alexander, K. (2023). Wind power fundamentals. In *Wind energy engineering: A handbook for onshore and offshore wind turbines*. Elsevier. <https://doi.org/10.1016/B978-0-323-99353-1.00007-4>
- Allik, A., Uiga, J., & Annuk, A. (2014). Deviations between wind speed data measured with nacelle-mounted anemometers on small wind turbines and anemometers mounted on measuring masts. <https://api.semanticscholar.org/CorpusID:73661171>
- Anderson, P. S., Ladkin, R. S., & Renfrew, I. A. (2005). An autonomous Doppler sodar wind profiling system. *Journal of Atmospheric and Oceanic Technology*, 22(9), 1309-1325. <https://doi.org/10.1175/JTECH1779.1>
- Andrews, J., Jelley, N. A., & Jelley, N. (2022). Wind power. In *Energy science: principles, technologies, and impacts*. Oxford university press.
- Barry, R. G., & Chorley, R. J. (2009). *Atmosphere, weather and climate*. Routledge.
- Barthelmie, R. J., Hansen, K., Frandsen, S. T., Rathmann, O., Schepers, J., Schlez, W., Phillips, J., Rados, K., Zervos, A., & Politis, E. (2009). Modelling and measuring flow and wind turbine wakes in large wind farms offshore. *Wind Energy: An International Journal for Progress and Applications in Wind Power Conversion Technology*, 12(5), 431-444. <https://doi.org/10.1002/we.348>
- Barthelmie, R. J., & Jensen, L. (2010). Evaluation of wind farm efficiency and wind turbine wakes at the Nysted offshore wind farm. *Wind Energy*, 13(6), 573-586. <https://doi.org/10.1002/we.408>
- Bechrakis, D., & Sparis, P. (2000). Simulation of the wind speed at different heights using artificial neural networks. *Wind Engineering*, 24(2), 127-136. <https://doi.org/10.1260/0309524001495503>
- Beck, H., & Kühn, M. (2017). Dynamic data filtering of long-range Doppler LiDAR wind speed measurements. *Remote Sensing*, 9(6), 561.
- Behrendt, A., Nakamura, T., Onishi, M., Baumgart, R., & Tsuda, T. (2002). Combined Raman lidar for the measurement of atmospheric temperature, water vapor, particle extinction coefficient, and particle backscatter coefficient. *Applied Optics*, 41(36), 7657-7666. <https://doi.org/10.1364/AO.41.007657>
- Berge, E., Gravdahl, A. R., Schelling, J., Tallhaug, L., & Undheim, O. (2006). Wind in complex terrain. A comparison of WAsP and two CFD-models. Proceedings from EWEC,
- Betz, A. (1926). *Wind-energie und ihre ausnutzung durch windmühlen* (Vol. 2). Vandenhoeck & Ruprecht.

- Bilal, M. (2016). Wind Energy at Nygårdstjernet–Norway. Wind field characterization and modelling.
- Bingöl, F., Mann, J., & Foussekis, D. (2009). Conically scanning lidar error in complex terrain. *Meteorologische Zeitschrift (Berlin)*, 18. <https://doi.org/10.1127/0941-2948/2009/0368>
- Bitsuamlak, G., Stathopoulos, T., & Bédard, C. (2004). Numerical evaluation of wind flow over complex terrain. *Journal of Aerospace Engineering*, 17(4), 135-145. [https://doi.org/10.1061/\(ASCE\)0893-1321\(2004\)17:4\(135\)](https://doi.org/10.1061/(ASCE)0893-1321(2004)17:4(135))
- Bjugg, M. (2023). *Wind resource assessment and siting for the expansion of Fakken wind park* UiT The Arctic University of Norway]. <https://hdl.handle.net/10037/30435>
- Bonin, T. A., & Brewer, W. A. (2017). Detection of range-folded returns in Doppler lidar observations. *IEEE Geoscience and Remote Sensing Letters*, 14(4), 514-518. <https://doi.org/10.1109/LGRS.2017.2652360>
- Bradley, S., Strehz, A., & Emeis, S. (2015). Remote sensing winds in complex terrain—a review. <https://doi.org/10.1127/metz/2015/0640>
- Carvalho, D., Rocha, A., Santos, C. S., & Pereira, R. (2013). Wind resource modelling in complex terrain using different mesoscale–microscale coupling techniques. *Applied Energy*, 108, 493-504. <https://doi.org/10.1016/j.apenergy.2013.03.074>
- Chavan, D. S., Saahil, V., Singh, A., Parashar, D., Gaikwad, S., Sankpal, J., & Karandikar, P. (2017). Application of wind rose for wind turbine installation. 2017 International Conference on Circuit, Power and Computing Technologies (ICCPCT),
- Christian, W. (2005). Doppler wind lidar. In *Lidar: range-resolved optical remote sensing of the atmosphere* (pp. 325-354). Springer.
- Christiane, D. (2024). Characterizing the convective boundary layer with wind-profiling and scanning Doppler lidar.
- Clifton, A., Clive, P., Gottschall, J., Schlipf, D., Simley, E., Simmons, L., Stein, D., Trabucchi, D., Vasiljevic, N., & Würth, I. (2018). IEA Wind Task 32: Wind lidar identifying and mitigating barriers to the adoption of wind lidar. *Remote Sensing*, 10(3), 406. <https://doi.org/10.3390/rs10030406>
- Emeis, S., Schafer, K., & Munkel, C. (2008). Surface-based remote sensing of the mixing-layer height—a review. *Meteorologische Zeitschrift*, 17(5), 621. <https://doi.org/10.1127/0941-2948/2008/0312>
- Fernando, H., Mann, J., Palma, J., Lundquist, J. K., Barthelmie, R. J., Belo-Pereira, M., Brown, W., Chow, F., Gerz, T., & Hocut, C. (2019). The Perdigo: peering into microscale details of mountain winds. *Bulletin of the American Meteorological Society*, 100(5), 799-819. <https://doi.org/10.1175/BAMS-D-17-0227.1>
- Frandsen, S., Barthelmie, R., Pryor, S., Rathmann, O., Larsen, S., Højstrup, J., & Thøgersen, M. (2006). Analytical modelling of wind speed deficit in large offshore wind farms. *Wind Energy: An International Journal for Progress and Applications in Wind Power Conversion Technology*, 9(1 - 2), 39-53. <https://doi.org/10.1002/we.189>
- Gasch, R., & Twele, J. (2011a). Historical development of windmills. In *Wind power plants: fundamentals, design, construction and operation*. Springer Science & Business Media. https://doi.org/10.1007/978-3-642-22938-1_2
- Gasch, R., & Twele, J. (2011b). The wind. In *Wind power plants: fundamentals, design, construction and operation*. Springer Science & Business Media. https://doi.org/10.1007/978-3-642-22938-1_4

- Giorgos, S. (2022). Rotor Blade Design, Number of Blades, Performance Characteristics. In *Handbook of Wind Energy Aerodynamics* (pp. 123-149). Springer. https://doi.org/https://doi.org/10.1007/978-3-030-31307-4_4
- González-Longatt, F., Wall, P., & Terzija, V. (2012). Wake effect in wind farm performance: Steady-state and dynamic behavior. *Renewable energy*, 39(1), 329-338. <https://doi.org/10.1016/j.renene.2011.08.053>
- González, J. S., Payán, M. B., Santos, J. M. R., & González-Longatt, F. (2014). A review and recent developments in the optimal wind-turbine micro-siting problem. *Renewable and sustainable energy reviews*, 30, 133-144. <https://doi.org/10.1016/j.rser.2013.09.027>
- Hakstok, I., & Mihajlović, Ž. (2014). Visualization of meteorological data. 2014 37th International Convention on Information and Communication Technology, Electronics and Microelectronics (MIPRO),
- Harris, M., Locker, I., Douglas, N., Girault, R., Abiven, C., & Brady, O. (2010). Validated adjustment of remote sensing bias in complex terrain using CFD. European Wind Energy Conference,
- Hasager, C. B., Nygaard, N. G., Volker, P. J., Karagali, I., Andersen, S. J., & Badger, J. (2017). Wind farm wake: The 2016 Horns Rev photo case. *Energies*, 10(3), 317. <https://doi.org/10.3390/en10030317>
- Holton, J. R. (2004). *An introduction to dynamic meteorology* (4th ed., Vol. 88). Elsevier Academic press.
- Huleihil, M., & Mazor, G. (2012). Wind turbine power: The betz limit and beyond. In *Advances in wind power*. IntechOpen. <https://doi.org/10.5772/52580>
- IEA. (2024). *Renewables 2023*. <https://www.iea.org/reports/renewables-2023>
- Jackson, P. L., & Steyn, D. G. (1994). Gap winds in a fjord. Part I: Observations and numerical simulation. *Monthly Weather Review*, 122(12), 2645-2665. [https://doi.org/10.1175/1520-0493\(1994\)122<2645:GWIAFP>2.0.CO;2](https://doi.org/10.1175/1520-0493(1994)122<2645:GWIAFP>2.0.CO;2)
- Jensen, N. O. (1983). *A note on wind generator interaction*. Risø National Laboratory.
- Jing, S., & Ergin, E. (2023). Estimation of wind energy potential and prediction of wind power. In *Wind energy engineering: A handbook for onshore and offshore wind turbines*. Elsevier. <https://doi.org/10.1016/B978-0-323-99353-1.00027-X>
- Julia, G. (2022). Wake Measurements with Lidar. In *Handbook of Wind Energy Aerodynamics* (pp. 1128-1143). Springer. https://doi.org/10.1007/978-3-030-31307-4_55
- Katic, I., Højstrup, J., & Jensen, N. O. (1987). A simple model for cluster efficiency. European wind energy association conference and exhibition,
- Khair, U., Fahmi, H., Al Hakim, S., & Rahim, R. (2017). Forecasting error calculation with mean absolute deviation and mean absolute percentage error. *journal of physics: conference series*,
- Kim, D., Kim, T., Oh, G., Huh, J., & Ko, K. (2016). A comparison of ground-based LiDAR and met mast wind measurements for wind resource assessment over various terrain conditions. *Journal of Wind Engineering and Industrial Aerodynamics*, 158, 109-121. <https://doi.org/10.1016/j.jweia.2016.09.011>
- Koch, F., Gresch, M., Shewarega, F., Erlich, I., & Bachmann, U. (2005). Consideration of wind farm wake effect in power system dynamic simulation. 2005 IEEE Russia Power Tech,

- Köpp, F., Rahm, S., & Smalikho, I. (2004). Characterization of aircraft wake vortices by 2- μ m pulsed Doppler lidar. *Journal of Atmospheric and Oceanic Technology*, 21(2), 194-206. [https://doi.org/10.1175/1520-0426\(2004\)021<0194:COAWVB>2.0.CO;2](https://doi.org/10.1175/1520-0426(2004)021<0194:COAWVB>2.0.CO;2)
- Krutova, M., Bakhoday-Paskyabi, M., Reuder, J., & Nielsen, F. G. (2022). Development of an automatic thresholding method for wake meandering studies and its application to the data set from scanning wind lidar. *Wind Energy Science*, 7(2), 849-873. <https://doi.org/10.5194/wes-7-849-2022>
- Lanchester, F. W. (1915). A contribution to the theory of propulsion and the screw propeller. *Journal of the American Society for Naval Engineers*, 27(2), 509-510.
- Lang, S., & McKeogh, E. (2011). LIDAR and SODAR Measurements of Wind Speed and Direction in Upland Terrain for Wind Energy Purposes. *Remote Sensing*, 3(9), 1871-1901. <https://doi.org/10.3390/rs3091871>
- Leosphere. (2023). WINDCUBE 100S/200S/400S - Hardware User Manual. In L. Windcube (Ed.), (pp. 44).
- Letcher, T. M. (2023). Why wind energy. In *Wind energy engineering: A handbook for onshore and offshore wind turbines*. Elsevier. <https://doi.org/10.1016/B978-0-323-99353-1.00025-6>
- Maiman, T. H. (1960). Stimulated optical radiation in ruby. *Nature*(187), 493–494. <https://doi.org/10.1038/187493a0>
- Mann, J., Angelou, N., Arnqvist, J., Callies, D., Cantero, E., Arroyo, R. C., Courtney, M., Cuxart, J., Dellwik, E., & Gottschall, J. (2017). Complex terrain experiments in the new european wind atlas. *Philosophical Transactions of the Royal Society A: Mathematical, Physical and Engineering Sciences*, 375(2091), 20160101. <https://doi.org/10.1098/rsta.2016.0101>
- Mann, J., Cariou, J.-P., Courtney, M., Parmentier, R., Mikkelsen, T., Wagner, R., Lindelöw, P. J. P., Sjöholm, M., & Enevoldsen, K. (2009). Comparison of 3D turbulence measurements using three staring wind lidars and a sonic anemometer. *Meteorologische Zeitschrift*, 18(2), 135-140. <https://doi.org/10.1127/0941-2948/2009/0370>
- Manwell, J. F., McGowan, J. G., & Rogers, A. L. (2010a). Introduction: Modern Wind Energy and its Origins. In *Wind energy explained: theory, design and application*. John Wiley & Sons. <https://doi.org/10.1002/9781119994367>
- Manwell, J. F., McGowan, J. G., & Rogers, A. L. (2010b). Wind Characteristics and Resources. In *Wind energy explained: theory, design and application*. John Wiley & Sons. <https://doi.org/10.1002/9781119994367>
- Manwell, J. F., McGowan, J. G., & Rogers, A. L. (2010c). Wind Turbine Siting, System Design, and Integration. In *Wind energy explained: theory, design and application*. John Wiley & Sons. <https://doi.org/10.1002/9781119994367>
- Markowski, P., & Richardson, Y. (2011). Blocking of the Wind by Terrain. In *Mesoscale meteorology in midlatitudes* (pp. 343-366). John Wiley & Sons, Ltd.
- Martin, J. E. (2006). *Mid-latitude atmospheric dynamics: a first course*. John Wiley & Sons.
- McClung, F. J., & Hellwarth, R. W. (1962). Giant optical pulsations from ruby. *Applied Optics*, 1(101), 103-105. <https://doi.org/10.1364/AO.1.S1.000103>
- Menke, R., Vasiljević, N., Wagner, J., Oncley, S. P., & Mann, J. (2019). Multi-lidar wind resource mapping in complex terrain. *Wind Energy Science Discussions, 2019*, 1-21. <https://doi.org/10.5194/wes-5-1059-2020>
- Mikkelsen, T. (2014). *Lidar-based Research and Innovation at DTU Wind Energy – a Review* Journal of Physics: Conference Series, Copenhagen, Denmark.

- National, R. C. (1992). Coastal meteorology: a review of the state of the science. <https://doi.org/10.17226/1991>
- Neto, J. D., & Castelao, G. P. (2023). lidarwind: A Python package for retrieving wind profiles from Doppler lidar observations. *Journal of Open Source Software*, 8(82), 4852. <https://doi.org/10.21105/joss.04852>
- Norgeskart. (2023). *Terrain Map*. Retrieved 20.11.2023 from <https://norgeskart.no/#!?project=norgeskart&layers=1004&zoom=8&lat=7794812.65&lon=682660.99&markerLat=7784846.216931002&markerLon=692661.5862953743&p=Koordinater&showSelection=false&sok=Hundhammarfjellet>
- Panwar, N. L., Kaushik, S. C., & Kothari, S. (2011). Role of renewable energy sources in environmental protection: A review. *Renewable and sustainable energy reviews*, 15(3), 1513-1524. <https://doi.org/10.1016/j.rser.2010.11.037>
- Persson, A. (1998). How do we understand the Coriolis force? *Bulletin of the American Meteorological Society*, 79(7), 1373-1386. [https://doi.org/10.1175/1520-0477\(1998\)079<1373:HDWUTC>2.0.CO;2](https://doi.org/10.1175/1520-0477(1998)079<1373:HDWUTC>2.0.CO;2)
- Petersen, E. L., Mortensen, N. G., Landberg, L., Højstrup, J., & Frank, H. P. (1997). Wind power meteorology. [https://doi.org/10.1002/\(SICI\)1099-1824\(199804\)1:1+<25::AID-WE4>3.0.CO;2-D](https://doi.org/10.1002/(SICI)1099-1824(199804)1:1+<25::AID-WE4>3.0.CO;2-D)
- Rathmann, O., Frandsen, S. T., & Barthelmie, R. J. (2007). Wake modelling for intermediate and large wind farms. 2007 European wind energy conference and exhibition,
- Ray, M., Rogers, A., & McGowan, J. (2006). Analysis of wind shear models and trends in different terrains. *University of Massachusetts, Department of Mechanical and Industrial Engineering, Renewable Energy Research Laboratory*.
- Reitebuch, O., & Hardesty, R. M. (2021). Doppler Wind Lidar. *Handbook of Atmospheric Measurements*, 759-797. https://doi.org/10.1007/978-3-030-52171-4_27
- Renfrew, I. A., & Anderson, P. S. (2006). Profiles of katabatic flow in summer and winter over Coats Land, Antarctica. *Quarterly Journal of the Royal Meteorological Society: A journal of the atmospheric sciences, applied meteorology and physical oceanography*, 132(616), 779-802. <https://doi.org/10.1256/qj.05.148>
- Risan, A., Lund, J. A., Chang, C.-Y., & Sætran, L. (2018). Wind in Complex Terrain—Lidar Measurements for Evaluation of CFD Simulations. *Remote Sensing*, 10(1), 59. <https://www.mdpi.com/2072-4292/10/1/59>
- Saheb, D., Koussa, M., & Hadji, S. (2014). Technical and economical study of a stand-alone wind energy system for remote rural area electrification in Algeria. *Renewable Energy and Power Quality Journal*, 1(12), 638-643. <https://doi.org/10.24084/repqj12.439>
- Sathe, A., & Mann, J. (2013). A review of turbulence measurements using ground-based wind lidars. *Atmospheric Measurement Techniques*, 6(11), 3147-3167. <https://doi.org/10.5194/amt-6-3147-2013>
- Schneemann, J., Trabucchi, D., Trujillo, J. J., & Kühn, M. (2014). Comparing measurements of the horizontal wind speed of a 2D Multi-Lidar and a cup anemometer. *Journal of Physics: Conference Series*,
- Scorer, R. (1952). Mountain - gap winds; a study of surface wind at Gibraltar. *Quarterly Journal of the Royal Meteorological Society*, 78(335), 53-61. <https://doi.org/10.1002/qj.49707833507>
- Shun, C., & Chan, P. (2008). Applications of an infrared Doppler lidar in detection of wind shear. *Journal of Atmospheric and Oceanic Technology*, 25(5), 637-655. <https://doi.org/10.1175/2007JTECHA1057.1>

- Smith, C. M., Barthelmie, R., Churchfield, M., & Moriarty, P. (2012). Complex wake merging phenomena in large offshore wind farms. 20th American Meteorological Society conference on boundary layers and turbulence, Boston, Massachusetts,
- Solbakken, K., & Birkelund, Y. (2018). Evaluation of the Weather Research and Forecasting (WRF) model with respect to wind in complex terrain. *Journal of Physics: Conference Series*,
- Solbakken, K., Birkelund, Y., & Samuelsen, E. M. (2021). Evaluation of surface wind using WRF in complex terrain: Atmospheric input data and grid spacing. *Environmental Modelling & Software*, 145, 105182. <https://doi.org/10.1016/j.envsoft.2021.105182>
- Spiridonov, V., Ćurić, M., Spiridonov, V., & Ćurić, M. (2021a). Atmospheric pressure and wind. *Fundamentals of Meteorology*, 87-114. https://doi.org/10.1007/978-3-030-52655-9_8
- Spiridonov, V., Ćurić, M., Spiridonov, V., & Ćurić, M. (2021b). Cyclones and Anticyclones. *Fundamentals of Meteorology*, 263-273. https://doi.org/10.1007/978-3-030-52655-9_17
- Stefan, E. (2018a). Statistical Tools. In *Wind energy meteorology: atmospheric physics for wind power generation*. Springer. <https://doi.org/10.1007/978-3-642-30523-8>
- Stefan, E. (2018b). Vertical Profiles Over Flat Terrain. In *Wind energy meteorology: atmospheric physics for wind power generation*. Springer. https://doi.org/10.1007/978-3-642-30523-8_3
- Stefan, E. (2018c). Winds in Complex Terrain. In *Wind energy meteorology: atmospheric physics for wind power generation*. Springer. https://doi.org/10.1007/978-3-642-30523-8_4
- Stull, R. B. (2017). *Practical meteorology: an algebra-based survey of atmospheric science* (Vol. 1.02b). University of British Columbia.
- Svendsen, H. S., H. R. (1995). Physical oceanography of coupled fjord-coast systems in northern Norway with special focus on frontal dynamics and tides. *Ecology of fjords and coastal waters*, 149-164.
- Texas, T. U. (2014). *Measuring the Complex Flows Found in Wind Plants*. Retrieved 03.06.2024 from <https://www.depts.ttu.edu/nwi/research/radar-research/>
- Thompson, R. D. (2002). *Atmospheric processes and systems*. Routledge. <https://doi.org/10.4324/9780203015872>
- Troms, K. (06.11.2023). *Fakken wind power plant*. Retrieved 06.11.2023 from <https://www.tromskraft.no/produksjon/kraftverk/fakken-vindkraftverk>
- Ulla, W. (2005). Introduction to Lidar. In *Lidar: range-resolved optical remote sensing of the atmosphere* (pp. 1-18). Springer.
- Van Der Tempel, J. (2006). *Design of support structures for offshore wind turbines*. Published and distributed by the author.
- van Dooren, M. F. (2022). Doppler Lidar Inflow Measurements. In *Handbook of Wind Energy Aerodynamics* (pp. 717-750). Springer. https://doi.org/10.1007/978-3-030-31307-4_35
- Varma, S. A. K., Srimurali, M., & Varma, S. V. K. (2013). Evolution of wind rose diagrams for RTPP, KADAPA, AP, India. *International Journal of Innovative Research and Development*, 2(13), 2278.
- Vasiljević, N., Vignaroli, A., Bechmann, A., & Wagner, R. (2020). Digitalization of scanning lidar measurement campaign planning. *Wind Energy Science*, 5(1), 73-87. <https://doi.org/10.5194/wes-5-73-2020>

- Vestas. (2007). *V90-3.0 MW An efficient way to more power*.
https://www.nhsec.nh.gov/projects/2008-04/documents/app_appendix_7.pdf
- Wallace, J. M., & Hobbs, P. V. (2006a). *Atmospheric Science: An Introductory Survey* (Vol. 92). Elsevier.
- Wallace, J. M., & Hobbs, P. V. (2006b). Atmospheric thermodynamics. In *Atmospheric Science: An Introductory Survey* (pp. 63-111).
- Wei, T. (2010). *Wind power generation and wind turbine design*. WIT press.
- WindSim. (2024). *WindSim technical brochure* Retrieved 03.06.2024 from
https://windsim.com/Windsimarchive/library%20--%20windsim-brochures/windsim_brochure_WEB.pdf
- Ying, A., & MD, P. (2005). A comparison of methods of extreme wind speed estimation. *Journal of Wind Engineering and Industrial Aerodynamics*, 93(7), 535-545.
<https://doi.org/10.1016/j.jweia.2005.05.003>
- Yoshino, K. (2019). Low-level wind shear induced by horizontal roll vortices at Narita International Airport, Japan. *Journal of the Meteorological Society of Japan. Ser. II*, 97(2), 403-421. <https://doi.org/10.2151/jmsj.2019-023>
- Zhao, F., Gao, Y., Wang, T., Yuan, J., & Gao, X. (2020). Experimental study on wake evolution of a 1.5 MW wind turbine in a complex terrain wind farm based on LiDAR measurements. *Sustainability*, 12(6), 2467. <https://doi.org/10.3390/su12062467>

Appendix B

The table below shows the turbine positions for Fakken I wind park in UTM34 and Longitude/Latitude coordinates.

Turbine Tag	UTM-zone 34W (eastx/northy)	Geographical degrees (Lat/Lon)
WTG01	463525/7776388	70.09171/20.04019
WTG02	463775/7776491	70.09267/20.04672
WTG03	464032/7776626	70.09392/20.05343
WTG04	464287/7776777	70.09531/20.06008
WTG05	464522/7776925	70.09667/20.06619
WTG06	464789/7776970	70.0971/20.07321
WTG07	465112/7777044	70.09781/20.08167
WTG08	465620/7777416	70.10122/20.09491
WTG09	462956/7776846	70.09574/20.02501
WTG10	463230/7776929	70.09652/20.03219
WTG11	463426/7776724	70.09471/20.03744
WTG12	463709/7777012	70.09733/20.04478
WTG13	463924/7777186	70.09892/20.05036
WTG14	464167/7777355	70.10047/20.05667
WTG15	464588/7777535	70.10214/20.06769
WTG16	464870/7777589	70.10267/20.0751
WTG17	465146/7777715	70.10383/20.08231
WTG18	465391/7777941	70.10589/20.08867

The table below shows the proposed turbine positions for Fakken II wind park in UTM34 and Longitude/Latitude coordinates.

Turbine Tag	UTM-zone 34W (eastx/northy)	Geographical degrees (Lat/Lon)
Turbine A	462658/7777193	70.09881/20.01702
Turbine B	462958/7777549	70.10204/20.02479
Turbine C	463574/7777494	70.10164/20.04101
Turbine D	463654/7777923	70.10549/20.04294
Turbine E	462042/7777367	70.10028/20.00075
Turbine F	462497/7777942	70.1055/20.01247
Turbine G	464082/7778204	70.10807/20.0541
Turbine H	461852/7777807	70.10419/19.99555
Turbine I	462169/7778350	70.10911/20.00367
Turbine J	462524/7778585	70.11127/20.01291
Turbine K	462858/7778251	70.10832/20.02186

